The Astronomical Journal, 136:2172–2200, 2008 November doi:10.1088/0004-6256/136/5/2172

SIMULATIONS OF THE DYNAMICAL AND LIGHT-SCATTERING BEHAVIOR OF SATURN'S RINGS AND THE DERIVATION OF RING PARTICLE AND DISK PROPERTIES

Carolyn C. Porco[1], John W. Weiss[1], Derek C. Richardson[2], Luke Dones[3], Thomas Quinn[4], and Henry Throop[5]
[1] CICLOPS/Space Science Institute, Boulder, CO 80301, USA; carolyn@ciclops.org
[2] University of Maryland, College Park, MD 20742, USA
[3] Southwest Research Institute, Boulder, CO 80302, USA
[4] University of Washington, Seattle, WA 98195, USA
[5] Southwest Research Institute, Boulder, CO 80302, USA
Received 2007 August 3; accepted 2008 September 2; published 2008 October 15

ABSTRACT

We study the light-scattering behavior of Saturn's rings for the purpose of deducing the nature and distribution of the particles comprising them and the collisional and dynamical environments in which they reside. To this end, we have developed two complex numerical codes to apply to this objective. One is a geometric ray-tracing code that scatters rays from a light source at an arbitrary illumination angle into a computer-generated patch of ring particles of predetermined photometric properties and size distribution, and counts the rays that emerge into arbitrary viewing directions. The code accounts for singly and multiply scattered light as well as the illumination of the rings by the planet Saturn. We examine the light-scattering behavior of various realizations of particle distribution, ring thickness, and optical depth—assuming macroscopic, backscattering particles with radii in the centimeter-to-meter range—and have compared our experimental results with classical analytical single-scattering and numerical multiple-scattering calculations, and with Cassini images of Saturn's A and C rings. We can reproduce the classical photometric results when vertically thick particle distributions are used, and we find good agreement with the observations when physically thin particle distributions are used, that is, in regimes where classical theory fails. This work has allowed us to demonstrate that the particles in the low optical depth portion of the C ring reflect about 32% of the incident sunlight in a manner similar to that of the jovian moon, Callisto. Those orbiting beyond the Encke gap in Saturn's A ring are nearly twice as reflective, and are slightly more forward scattering than those in the C ring. The A ring vertical full thickness beyond the Encke gap is likely to be very thin, ∼10 m. The thickness of the C ring is not discernible from this work. The optically thicker A and B rings are darker at high phase than classical calculations predict because they are so thin. We have also incorporated the capability to realistically simulate a patch of colliding, self-gravitating particles in Saturn's gravity field into a sophisticated N-body parallel tree code. This code can model dissipative collisions among several million particles with optional sliding friction. We have applied our light-scattering code to simulations of Saturn's A ring produced by this patch code in which gravitational wakes have been observed to form. We have demonstrated, as have others, that such wakes are the likely cause of the well-known azimuthal brightness asymmetry in Saturn's A ring. We match the asymmetry amplitude and shape, as observed primarily in low-solar-phase Voyager images, by assuming a velocity-dependent restitution law that yields a coefficient of restitution ∼3.5 times lower at the velocity dispersions appropriate for the smallest particles in Saturn's rings than previously assumed; Cassini data are consistent with these results. We simultaneously find a particle albedo and phase function consistent with those deduced from photometric analyses of Cassini images taken on approach to Saturn. These results suggest that the ring particle collisions in Saturn's A ring are more lossy than previously expected, a result possibly due to particle surface roughness, a regolith, and/or a large degree of porosity, all of which would lower the coefficient of restitution.

Key words: planets: rings – planets and satellites: individual (Saturn)

1. INTRODUCTION

Particle disks, such as planetary rings, of varying thicknesses differ in the manner in which they scatter light. Consequently, observations of a ring's light-scattering properties may in principle be used to infer the spatial and physical characteristics of the particles comprising it. The usual approach to this problem has utilized classical radiative transfer techniques, which strictly apply to many-particle-thick systems of randomly distributed particles. However, Saturn's rings do not necessarily fit this assumption. There are small-scale structures such as clumps and self-gravity wakes within them (e.g., Colwell et al. 2006), and there is good reason to believe that the rings may be very thin (e.g., Hedman et al. 2007), with a vertical thickness of only ∼6 m, comparable to the size of the largest particles, a circumstance under which the classical techniques have limited utility. Although much has already been inferred about the rings' properties and dynamics from observations, many studies have been hindered by an incomplete accounting for all of these conditions.

Modeling the light scattering within the rings may allow insight into key planetary ring problems, the solutions to some of which are still elusive. These problems include the following.

1. What is the vertical thickness of the rings? Both models (Brahic 1977; Goldreich & Tremaine 1982) and analysis and modeling of Cassini stellar occultation observations (Colwell et al. 2006; Hedman et al. 2007) suggest that Saturn's rings may be very thin, ∼6 m thick. The spatial resolution and geometry of past and future observations are inadequate to measure the rings' thickness directly, though Cassini can set stricter limits than are obtainable from either Voyager or ground-based observations. Estimates of the thickness are possible by studying

how rings of varying thicknesses scatter light and comparing this to observations of the rings' brightness.

2. Saturn's A ring has a well-known brightness asymmetry, in which the brightness around the ring changes with a quadrupole variation. How is this phenomenon produced? It has been proposed (e.g., Colombo et al. 1976) that it is due to self-gravity wakes in the rings, and Dones & Porco (1989) were the first to numerically investigate this possibility by applying a single scattering code to an idealized representation of a wake. Since then, others have followed suit, with ever more sophisticated numerical models (e.g., Salo 1992; Richardson 1994). However, quantitative studies linking the physical characteristics of the rings and their embedded self-gravity wakes with the observed characteristics of the brightness asymmetry are only now beginning (e.g., Salo et al. 2004a).

3. What causes the "opposition surge" in Saturn's rings? This effect, in which the rings' brightness surges dramatically at phase angles very near zero, has been observed in Saturn's rings in *Hubble Space Telescope* (*HST*; French et al. 2007b) and Cassini (Déau et al. 2008) images. The variation in ring brightness at small phase angles is thought to arise from a combination of physical optics effects between tiny surface grains ("coherent backscattering"), *intra*particle shadowing due to surface roughness on a variety of spatial scales, and *inter*particle shadowing between ring particles. The sharpness of the opposition effect due to interparticle shadowing depends on the thickness of the rings.

4. Saturn's rings are darker in near-forward scatter than radiative transfer multiple scattering calculations can reproduce, even if no small forward-scattering particles are assumed to be present in the rings.

5. How are ring brightness and optical depth correlated? While even classical theory predicts a strong correlation between the optical depth and ring brightness at high phase angles, the observed correlation between the optical depth and brightness at low-to-moderate phase angles is surprising. Furthermore, the correlation is present even when the lit face of the rings is viewed at shallow angles, a geometry in which classical calculations predict that the brightness should tend toward equality for both optically thin and thick regions.

6. The brightness of the B ring increases as the solar incidence angle and observer emission angle decrease at a constant phase angle, in contrast to what single-scattering models predict; this is the B ring "tilt effect." The opposite is true for the A ring (an "antitilt effect"), though previous work suggests that multiple scattering and the presence of self-gravity wakes in the A ring may be responsible for these effects (Salo & Karjalainen 2003; Salo et al. 2004a). Reproducing these photometric observations in light-scattering experiments by utilizing realistic simulations of Saturn's rings will provide insight into the rings' structure, dynamics, collisional environment, particle properties, and perhaps their evolutionary history.

This research involves the development and application of two complex computer codes. The first is an *N*-body scalable, parallel tree code that has been customized, using a "sliding patch" model, to simulate a patch of colliding, self-gravitating ring particles in Saturn's gravity field. The output of this code is a realistic, three-dimensional distribution of particle locations in a patch of the rings. Application of this code (as well as similar codes of other researchers in this field (e.g., Salo 1992, Daisaka et al. 2001) has demonstrated the existence of transient gravitational wakes in simulations of Saturn's A ring, the structures that are believed to be the source of the A ring brightness asymmetry.

The second code follows light rays into a computer-generated box of ring particles of predetermined photometric properties (such as those produced by the *N*-body patch code), and collects the rays that scatter off the particles and emerge into arbitrary viewing directions. The code accounts for singly and multiply scattered sunlight as well as the illumination of the rings by the planet Saturn, and can be applied to many photometric problems in planetary rings. The version described here does not model the effects of diffraction, though this is likely to be a small effect for the phase angles considered here.

We can also run the ray-tracing code on computer-generated boxes containing particles that are not placed via *N*-body simulations. For example, we can place the particles into idealized wakes to perform initial tests on models without running the time- and computation-expensive *N*-body code. Dones & Porco (1989) used a single-scattering code on a box of particles representing an idealized wake that had been constructed to mimic the surface mass density contours given by Julian & Toomre (1966) for a Keplerian velocity field, and produced the first demonstration that self-gravity wakes are the underlying cause of the azimuthal asymmetry. We can also randomly distribute particles in the horizontal plane but with a Gaussian distribution in the vertical dimension in order to investigate the light scattering of a ring patch in the absence of gravitational wakes. These experiments have allowed us to separate out the background scattering properties of the rings from those attributable to coherent structures like self-gravity wakes. They also allow us to compare our light-scattering results to results expected from classical treatments.

The work described herein is the beginning of a program to use our numerical methods to determine the physical and photometric properties of the particles in Saturn's rings and their three-dimensional distribution by modeling the rings' photometry. It will allow us to use the local variations in the spatial distribution of particles, and concomitantly the variation in light scattering, to probe the underlying ring structure and dynamics (e.g., examining the propeller features found in the A ring by Tiscareno et al. 2006) and the nature of the particles themselves. It will also allow us to set limits on the thickness of Saturn's rings in a variety of ring regions. This will be especially useful for unperturbed regions that cannot be probed by other methods, such as estimating the velocity dispersion from the damping length of density waves or measuring the vertical thickness at ring edges in either radio or stellar occultation observations made from spacecraft like Cassini.

In Section 2, we first describe the general formulation of the ray-tracing approach using both sunshine and sunlight reflected by the planet onto the rings (also called planetshine). In Section 3, we demonstrate the fidelity of the approach by examining the light-scattering behavior of various combinations of particle spatial distribution, size distribution, ring thickness, and optical depth, and then comparing these experimental results with classical analytical calculations, with tabulations of numerical results based on the standard "adding–doubling" method in radiative transfer (van de Hulst 1980), and with Cassini observations of Saturn's rings. We find good agreement with theory and with the published data, even in regimes where classical theory fails. In Section 3.3, we apply our technique to simulate the effect of planetshine on the lit and unlit sides of the B and C rings.

In Section 4, we describe the modifications of an existing *N*-body parallel tree code to incorporate a local shearing disk model to simulate the dynamics of a patch of Saturn's rings. This code, which can simulate a larger range and number of particles than other realistic *N*-body codes, readily produces ring patches that exhibit the transient self-gravity wakes predicted by Julian & Toomre (1966).

In Section 5, we apply our ray-tracing technique to realistic ring patch simulations, to model the azimuthal brightness variations seen in the mid-A ring in low-solar-phase Voyager and Cassini images. This photometric phenomenon in the A ring is well known (e.g., Lumme & Irvine 1976; Reitsema et al. 1976), and others have previously confirmed self-gravity wakes as the cause of it (e.g., Dones & Porco 1989; Salo et al. 2004a). We find that to reproduce the shape and the amplitude of the A ring light curve in low-phase, lit-face geometries requires a velocity-dependent coefficient of restitution that yields more energy loss at the velocity dispersions appropriate for the smallest particles in the rings than has heretofore been assumed. These results will prove significant in the evaluation of the transfer of angular momentum and energy across the rings, and in studies of ring age, evolution, and lifetime.

In Section 6, we summarize and discuss the significance of our results.

2. GENERAL FORMULATION

We consider spherical particles of various sizes distributed in a box, which mimics a "patch" in the ring plane. We work in the limit of geometric optics, that is, the particle radius r is much larger than the wavelength of light. In Saturn's main rings, the vast majority of ring particles are between 1 cm and 20 m (Zebker et al. 1985; French & Nicholson 2000); thus, our assumption is valid for images of the rings taken at visual, ultraviolet, and near-infrared (NIR) wavelengths. The particles are arranged in a three-dimensional box. The dimensions of the box are Δ_x, Δ_y, and Δ_z. The coordinate system x, y, z follows the right-hand rule x is radially outward, y is in the orbital direction, and z is north. The box has periodic boundary conditions in the x and y directions: that is, after exiting the side of the box, a ray can propagate through an identical box along its path until it finally hits a particle or emerges out of the bottom of the layer. The solar incidence angle is i, the observer emission angle is e, and both are measured from the normal of the box on the lit side. The incidence angle is, by definition, $\leqslant 90^\circ$; it is related to the solar elevation angle, θ_0, by $i = 90^\circ - \theta_0$ for $\theta_0 > 0$ and by $i = 90^\circ + \theta_0$ for $\theta_0 < 0$. The emission angle is related to the observer elevation angle, θ, by $e = 90^\circ - \theta$ for $\theta > 0$ and by $e = 90^\circ + \theta$ for $\theta < 0$. The emission angle can take on values between 0 and 180°. The quantities $\mu_0 = |\cos(i)|$ and $\mu = |\cos(e)|$ are defined for convenience. The locations of the Sun and observer are given as unit vectors from the origin of the box that is taken to be the box center.

The Sun-ring-observer angle is denoted by the phase angle, α, where $\alpha = 0^\circ$ corresponds to exact backscattering. The longitude λ is the planetocentric longitude of a point on the rings taken relative to the observer and in the direction of orbital motion, that is, the right-hand side of the northern side of the ring visible to an observer has $0^\circ < \lambda < 180^\circ$. The solar and observer azimuth angles are, respectively, ϕ_0 and ϕ and are measured in the same coordinate system. The albedo is A; we use this both for the Bond and single-scattering albedos. Both quantities indicate the fraction of energy reflected (and, in general, refracted) by a particle into all directions. It does not include light diffracted by the particle.

The angles i, e, θ_0, θ, μ_0, μ, and α relate the positions of the Sun, ring, and observer to each other. In the ray-tracing method, however, another set of equivalent angles must also be defined relative to the surface of individual particles, and not the ring plane, for each scattering event. For clarity, we will define the subscripted quantities i_s, e_s, θ_s, θ_{0s}, μ_{0s}, μ_s, and α_s to denote these same angles, taken with respect to the surface of the particle at the point of contact. For instance, i_s denotes the incidence angle of a ray relative to the surface normal at the point of scattering. This ray could come from either the Sun (single scattering) or another particle (multiple scattering), or Saturn (planetshine); the angles are defined in the same way for all cases.

The brightness of a patch of ring is expressed with the usual quantity I/F, where $I/F \equiv 1$ for a flat, white Lambertian surface illuminated at normal incidence viewed from any direction. Formally, I is the intensity measured from a surface illuminated with flux density πF. The reflectance I/F is a measure of the reflectivity of the surface, and is a function of illumination and observing geometry.

2.1. Particle Distributions

To describe the ring particles' size distribution, we use both unimodal and power-law size distributions in our simulations. For the power laws, we assume

$$n(r)\,dr = n_0 \left(\frac{r}{r_{\min}}\right)^{-q} dr, \tag{1}$$

where $n(r)\,dr$ is the volume number density of particles with radii between r and $r + dr$ and q is the power-law index. In Saturn's rings, $q \sim 3$ (Zebker et al. 1985; French & Nicholson 2000). When $q \sim 3$, for a normal optical depth, τ, a full ring thickness of h, and a uniform distribution in the direction perpendicular to the rings, the constant, n_0, becomes

$$n_0 = \begin{cases} \dfrac{\tau}{h\pi r_0^3} \dfrac{3-q}{(r_{\max}/r_{\min})^{3-q} - 1} & q \neq 3 \\ \dfrac{\tau}{h\pi r_0^3} \dfrac{1}{\ln(r_{\max}/r_{\min})} & q = 3 \end{cases}, \tag{2}$$

where $r_{\min}$ is the minimum particle size, $r_{\max}$ is the maximum, and we have assumed that all particles fall in the geometric optics regime. In this work, to reduce the numbers of particles, and hence the numbers of calculations, required to simulate the rings, we have considered particles from the tens of centimeters to ~5 m in radius, even though the particle size distribution in Saturn's A and B rings appears to span a broader size range from $r_{\min} \sim 30$ cm to $r_{\max} \sim 20$ m (French & Nicholson 2000). However, it should be noted that there is some debate about the reliability of the upper limit, as the presence of self-gravity wakes in some rings may cause the derived maximum particle size to be overestimated. Moreover, an upper limiting particle radius of ~5 m is more readily understandable on a theoretical basis, since this is the natural scale of self-gravitational disturbances expected in Saturn's rings and set by the differential angular velocity in Saturn's rings (Shu 1984).

2.2. Optical Depths

Several optical depths can be defined for rings. The physical optical depth τ_p is defined such that a "skewer," passed

perpendicularly through the ring, has a probability $e^{-\tau_p}$ of not intercepting a ring particle: that is, τ_p is the quantity that most directly relates to an observed I through the relation $I \sim I_0 e^{-\tau_p}$, where I_0 is the incident intensity and here I is the intensity of the attenuated direct beam. It depends on the spatial distribution of the particles. In creating simulated boxes of particles, it is impossible a priori to determine τ_p and it must, in general, be calculated numerically. Hence, boxes of all kinds used here, whether random or produced via dynamical simulations, are created with a prespecified *dynamical* optical depth, τ_d, which is the ratio of the total cross-sectional area of the particles to the topside area of the box (Wisdom & Tremaine 1988). That is, if h is the vertical thickness of the ring,

$$\tau_d = h \int_{r_{\min}}^{r_{\max}} \pi r^2 n(r)\, dr. \tag{3}$$

The ratio of physical to dynamical optical depth remains near unity until the optical depths grow larger than ∼1. For a completely filled box, the dynamical optical depth remains finite, but the physical optical depth becomes infinite. However, when there are pronounced variations in the spatial distribution of the particles, as there are in the presence of self-gravity wakes, the physical optical depth can in fact be less than the dynamical optical depth.

Another optical depth of interest in this problem is the "path optical depth," τ_{pa}, which accounts for the path length of a ray traveling into a ring, being scattered, and traveling out:

$$\tau_{pa} = \tau_p \left(\frac{1}{\mu} + \frac{1}{\mu_0} \right). \tag{4}$$

Throughout this paper, unless otherwise specified, an unsubscripted optical depth, τ, refers to dynamical optical depth.

2.3. Spatial Distributions

We use three different methods of spatially distributing our ring particles within a three-dimensional box before applying the ray-tracing code to them. These are (1) random, (2) dynamical, and (3) idealized wakes. The different distribution methods are useful in isolating different effects in Saturn's rings.

For the random distribution, we place particles into the box, one at a time. Particles are placed randomly in the x and y dimensions and are distributed randomly in the z direction but according to an overall Gaussian distribution; the ring's thickness is specified by σ_z, the standard deviation of the distribution. (This can be converted into full width at half-maximum (FWHM) by multiplying by $2\sqrt{2\ln(2)} \approx 2.35$.) Roughly, 68% of the particles in these boxes lie within $\pm 1\sigma_z$ of the midplane. We add particles to the distribution until the desired dynamical optical depth is achieved, taking care to ensure that particles do not physically overlap each other.

Particle positions in the "dynamical" simulations are determined by the output of our N-body collisional, self-gravitational numerical ring model. This distribution is a snapshot of a patch of a ring. We defer a complete discussion to Section 4, but note that this patch code produces the self-gravity wakes inferred to exist in the A ring and at some locales in the B ring.

In some cases, especially when exploring parameter space, rather than run the N-body code, which can be time consuming, we construct "idealized wakes" by placing particles along lines with a specified separation and pitch angle to the orbital direction. We can also specify how the particles are distributed around the specified wake axis by altering the width or thickness of the wakes. The resulting idealized structures are roughly cylinders with an elliptical cross section. While they lack the smaller-scale morphology seen in N-body simulations, they provide an efficient way to examine the effects of wakes on photometry.

2.4. Surface Properties and Phase Functions

The phase function $P(\alpha)$ describes the angular dependence of the scattering of light by a particle. It is normalized such that

$$\left(\frac{1}{4\pi}\right) \int_0^{2\pi} \int_0^{\pi} P(\alpha) \sin(\alpha)\, d\alpha\, d\phi = 1, \tag{5}$$

where ϕ is the azimuthal angle measured around the direction to the Sun. The integral, which is taken over all solid angles, is an expression of conservation of flux.

We consider five phase functions to model the particles' light -scattering behavior, shown in Figure 1. The first, a Lambert phase function, models the light reflected from a smooth, opaque sphere. The second was an empirical fit to the surface of the jovian moon, Callisto, by Squyres & Veverka (1981). This phase function has a weak opposition surge (i.e., brightening near $\alpha = 0^\circ$ that is not as pronounced as the rings' opposition surge). We describe its implications in Section 3.2.2. (Note that the term "Callisto phase function" has had several different meanings in the literature. For example, Dones et al. (1993) used it to mean either a power-law phase function with $n \sim 3$ (Equation (11)) or the Squyres and Veverka fit. In this paper, however, we use the term to mean the Squyres and Veverka fit *exclusively* in order to avoid confusion.) Third, we employ two power-law phase functions derived from the photometric modeling of Voyager images (Dones et al. 1993). Finally, we consider an isotropic phase function. Although the rings are not well modeled by isotropic scatterers, this phase function is used in many multiple-scattering codes, is found in the literature, and provides a useful comparison and check on our calculations.

Our ray-tracing method calculates I/F (the ring reflectivity for a given geometry) based on the reflectivity $\rho_s(\alpha_s)$ of a particle surface, while the classical analytic equations for single-scattering (Section 2.5) and classical multiple-scattering codes use the disk-integrated phase function $P(\alpha)$. (Here, we mean the "disk" of a particle, treating it as if it were a planet.) Use of the disk-integrated phase function implies a particle being illuminated by a wide beam of rays that samples every point on the surface. In our ray-tracing code, however, particles are hit by discrete rays. As a result, the function describing the angular dependence of the reflected brightness is not averaged over all incidence angles, μ_0, on the curved lit hemisphere of a particle. Instead, the ray strikes the surface at one point, and the scattering event is characterized by a unique incidence angle from the normal to the surface, μ_{0s}, and a unique emission angle, μ_s.

Therefore, we must distinguish between the disk-integrated phase function $P(\alpha)$ and the surface reflectivity $\rho_s(\alpha_s)$, where α_s is the angle between the incoming and outgoing rays *at the point of contact on the surface.* The relationship between these quantities was discussed by Squyres & Veverka (1981).

With these distinctions in mind, we have

Lambert:

$$\rho_s(\alpha_s, \mu_s, \mu_{0s}) = \begin{cases} 1 & \mu_{0s} \geqslant 0 \\ 0 & \mu_{0s} < 0 \end{cases} \tag{6}$$

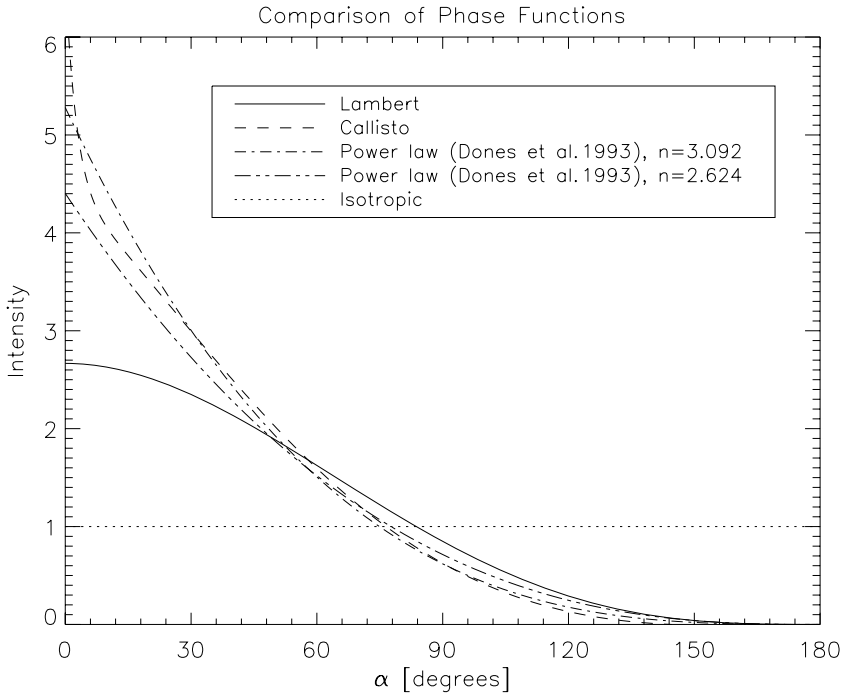

Figure 1. The five phase functions used in this work: Lambertian, isotropic, and the empirically determined phase functions: Callisto (Squyres & Veverka 1981) and two power-law functions with indices of 2.624 and 3.092 (Dones et al. 1993). Except very near 0° phase, the $n = 3.092$ power law is very similar to the Callisto function, making the two difficult to distinguish in practice outside the opposition surge.

$$P(\alpha) = \frac{8}{3\pi}[\sin\alpha + (\pi - \alpha)\cos\alpha]. \quad (7)$$

Callisto:

$$\rho_s(\alpha_s, \mu_s, \mu_{0s}) = \begin{cases} \frac{1.1}{\mu_{0s}+\mu_s}(2 - 0.79333\,\alpha_s + e^{-21.2\alpha_s}) \\ 0 \end{cases} \quad (8)$$

$$P(\alpha) = \begin{cases} 2.2(2 - 0.79333\,\alpha + e^{-21.2\alpha})\left(1 + \sin\left(\frac{\alpha}{2}\right)\right. \\ \quad \left. \times \tan\left(\frac{\alpha}{2}\right)\ln\left(\tan\left(\frac{\alpha}{4}\right)\right)\right) \\ 0 \end{cases}. \quad (9)$$

The upper options in Equations (8) and (9) apply only for $\alpha_s \lesssim 2.521$ rad (144.°3); the lower options apply for $\alpha_s \gtrsim 2.521$ rad (144.°3).

Power law:

$$\rho_s(\alpha_s, \mu_s, \mu_{0,s}) = \frac{3\pi}{8}\frac{c_n(\pi - \alpha)^n}{\sin(\alpha) + (\pi - \alpha)\cos(\alpha)}, \quad (10)$$

$$P(\alpha) = c_n(\pi - \alpha)^n, \quad (11)$$

where the normalization constants, c_n, are tabulated for some values of the index n (a positive real number) in Dones et al. (1993, Table IV). (For example, for $n = 3.092$, Dones et al. 1993 gave $c_n = 0.153$.) Equation (10) is derived by insisting that when the surface reflectivity is integrated over the entire disk of the particle, the phase function described by Equation (11) results. There are an infinite number of such reflectivities for a given phase function. We chose one that assumes that ρ_s is independent of μ_s and μ_{s0}. The derived reflectivity has been validated by checking that it gives the same results as the classical, analytical calculations when the power-law phase function is used.

Isotropic:

$$\rho_s = 1/(4\mu_s) \quad (12)$$

$$P = 1. \quad (13)$$

This isotropic phase function is used only to validate our results against those of van de Hulst (1980), whose primary purpose was to study scattering in planetary atmospheres. It is not technically appropriate for ring particles since the surface reflectivity, ρ_s, derived from it necessarily yields a function that sends rays *through* the scattering particle, unlike the other three phase functions we use. We include the isotropic phase function here for completeness.

A truly realistic light-scattering code would take into account the wave nature of light and consider the contributions of diffraction. In reality, the net effect of diffraction on the emerging I/F is difficult to calculate in the most general case. However, throughout this investigation, we only consider particles much larger than the wavelength of light. In this case, diffraction has the effect of removing photons from an incident beam hitting the particle and redirecting them into a very narrow, forward-scattered beam (Cuzzi 1985; Roques et al. 1987). For the geometries we consider here (i.e., far from $\alpha = 180°$), we can safely neglect diffraction. Also, though it is not strictly true in all scenarios considered here, we assume that the particles do not fall within each other's diffraction lobes. Under these assumptions, diffraction is likely to be a small contributor and can be neglected.

2.5. Calculation of Scattered Intensity: Analytic Single-Scattering

We use the standard radiative transfer equations to calculate the I/F under "classical" conditions, using as input parameters

the scattering geometry and the ring's particle and disk properties. These methods allow us to verify our calculations for rings described by multiparticle-thick boxes of well-separated particles at low-to-intermediate phase angles. (At these phase angles, the rings' reflectivity is generally dominated by single scattering; Dones et al. 1993.) Following Chandrasekhar (1950), the diffuse scattering function S was applied to the case where θ and θ_0 had the same sign: that is, on the same side of the ring plane (his Equation VII.35)

$$S = AP(\alpha)\left[1 - \exp\left[-\tau\left(\frac{1}{\mu} + \frac{1}{\mu_0}\right)\right]\right] \Big/ \left(\frac{1}{\mu} + \frac{1}{\mu_0}\right). \quad (14)$$

The corresponding diffuse transmission function T, where θ and θ_0 have opposite signs, is given by (again, Chandrasekhar's Equation VII.35)

$$T = AP(\alpha)\left[e^{-\tau/\mu_0} - e^{-\tau/\mu}\right] / \left(\frac{1}{\mu} - \frac{1}{\mu_0}\right), \quad (15)$$

when $\mu \neq \mu_0$.

The reflected brightness of a patch of ring is given by

$$\frac{I}{F}(A, \alpha, \mu_0, \mu, \tau) = \frac{AP(\alpha)}{4}\frac{\mu_0}{(\mu_0 + \mu)} \times \left[1 - \exp\left(-\tau\,\frac{\mu + \mu_0}{\mu\mu_0}\right)\right] \quad (16)$$

and the diffusely transmitted brightness is

$$\frac{I}{F}(A, \alpha, \mu_0, \mu, \tau) = \frac{AP(\alpha)}{4}\frac{\mu_0}{|\mu - \mu_0|}\left[e^{-\tau/\mu} - e^{-\tau/\mu_0}\right], \quad (17)$$

when $\mu \neq \mu_0$.

Equations (16) and (17) define our classical, analytic calculations. Because these equations account for single scattering only, they are guaranteed to work well only along paths where $\tau/\mu \ll 1$, $\tau/\mu_0 \ll 1$, and $A \ll 1$. However, it turns out that the reflectivity of the lit face of Saturn's main rings is dominated by single scattering at phase angles less than about 60° (Doyle et al. 1989; Dones et al. 1993), so they come close to reproducing the brightness of Saturn's rings in this geometry.

2.6. Calculation of Scattered Intensity: Ray Tracing

Calculation of the brightness of a ring of many scatterers distributed arbitrarily in three dimensions requires a numerical ray-tracing approach. Our ray-tracing code follows the path of a large number, N, of independent rays originating from a source and impinging, all at the same incidence angle, on the top of a box of known dimensions. The rays enter the particle box at evenly-spaced grid points. When a ray encounters a particle, it is split up into n_c child rays, distributed in a solid angle (Figure 2) and each with a brightness reduced according to the albedo, phase function of the surface, and the number of child rays. These rays are then propagated forward in space.

Our code can handle an arbitrary scattering order, but for computational efficiency, we generally limit the calculations to the fourth order: that is, no more than four successive scatterings are considered. (In practice, we check the contribution of the last scattering order. If it is small ($\simeq$1%), it is assumed that higher orders of scattering $\geqslant$2 will be significantly smaller and thus negligible.)

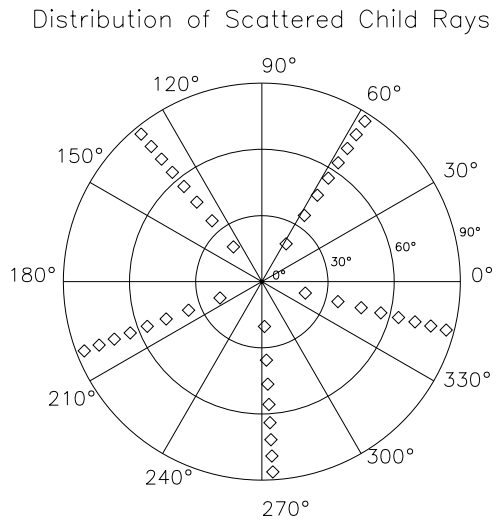

Figure 2. Angular distribution of outgoing child rays from the primary particle. The number of rays is changeable, but almost all ray-tracing runs in this work have used the 40 shown here. This polar plot shows the zenith angle radially. The child rays are evenly spaced in azimuth, but are spaced in altitude so that each ray represents an equal solid angle seen from the particle's surface. Additionally, the azimuths are started from 1 rad rather than 0 rad to avoid sending rays off exactly in the x–y plane. (Such rays can never escape the particle box without scattering and thus are prone to extend run times significantly, especially at low optical depths.)

Because the odds that one of the rays scattered according to Figure 2 will head toward the observer (even with a reasonable field of view) are extremely small, an additional ray is scattered toward the observer at each scattering event. This ray is not a true "child" ray in that it cannot initiate a cascade of its own child rays upon striking a particle. It is there merely to ensure that the contribution of any scattering event to the observed intensity is recorded in the event that the point of scattering on the particle's surface is viewable by the observer but no child ray is.

Our ray-tracing method is entirely deterministic; there are no random numbers drawn to determine which ray is followed. Given a scattering geometry, phase function, and particle distributions in size and space, the number of collected rays at the observer depends only on the number N of source rays used, the order n of scattering, and the number of child rays, n_c, created per multiple-scattering event. Increasing all these parameters increases both accuracy and execution time. Typically, the grid size and, therefore, the number N, are chosen so that, on average, each particle is hit by at least one ray. In cases where large numbers of very small particles exist, it becomes impractical to stick to this rule of thumb, so we chose a grid size suitable for particles in the middle of the size distribution. Thus, our grid spacing is typically of order of a meter.

Generally, the I/F of a surface is given by

$$\left(\frac{I}{F}\right) = A\rho_s(\alpha_s, \mu_s, \mu_{0s})\mu_{0s}. \quad (18)$$

However, our method traces the paths of individual rays. These are not spread across the surface of the particle like an incident broad beam of rays would be, so the factor of μ_{0s} is not applicable. Furthermore, because we calculate the intensity of each scattered ray and not the I/F of the surface, a factor of μ_s/π is required in order to convert from the usual surface I/F to intensity (van de Hulst 1980, p. 600).

Therefore, the contribution to the intensity, I, seen by an unobscured observer after the scattering of a source ray, denoted

by k, is

$$I_k^{(1)} = I_k^{(0)} A \rho_s(\alpha_s, \mu_s, \mu_{0s}) \frac{\mu_s}{\pi}. \quad (19)$$

The intensity of an incident ray is defined as $I^{(0)} \equiv 1$ for solar illumination. In this case, the total incident intensity on the ring patch, F, is N, the number of rays.

If only single scattering is considered, then the I/F for the ring patch is given by

$$\left(\frac{I}{F}\right) = \frac{\mu_0}{\mu} \frac{\pi}{N} \sum_{k=1}^{N} I_k^{(1)}, \quad (20)$$

where, if the line of sight to the observer is blocked by another particle, $I_k^{(1)} = 0$ (e.g., the ray does not contribute to the final I/F since it is obscured).

In the multiple-scattering case, at each scattering event the flux is divided among the n_c child rays. Child rays are distributed across n_ϕ azimuths and n_θ altitudes relative to the point on the particle's surface, so that $n_c = n_\phi n_\theta$. In the azimuthal direction, child rays are evenly spaced. The n_ϕ rays at the ith altitude have altitude

$$\theta_s(i) = \arcsin\left(\frac{2i+1}{2n_\theta}\right) \quad (21)$$

so that each child ray represents an equal solid angle of the sky seen from the particle's surface.

Each emerging ray is reduced in brightness by factors accounting for the albedo and the surface reflectivity function so that the total flux of the child rays equals the flux of the parent times the surface albedo. Each child ray is propagated forward in its new direction until it either impacts another particle or leaves the box. At the next encounter, the intensity of one of the reflected child rays seen by the observer is

$$I_k^{(2)} = \frac{\mu_s^{(2)}}{\pi} I_k^{(1)} A \rho_s\left(\alpha_s^{(2)}, \mu_s^{(2)}, \mu_{0s}^{(2)}\right). \quad (22)$$

The process is repeated for higher orders of scattering, where the brightness of a reflected child ray at each scattering event is given by

$$I_k^{(n)} = I_k^{(n-1)} A \rho_s\left(\alpha_s^{(n)}, \mu_s^{(n)}, \mu_{0s}^{(n)}\right) \frac{\mu_s^{(n)}}{\pi}. \quad (23)$$

We calculate the contributions from a source ray, k, and its cascade of child rays to the I/F seen by an observer by summing the intensities from all the scattering events in the cascade, which finally make it to the observer. By dividing by F, we obtain our final result:

$$\left(\frac{I}{F}\right) = \pi \frac{1}{N} \left[I_k^{(1)} + \sum_{i=1}^{n_c} I_{i,k}^{(2)} + \cdots + \sum_{i=1}^{n_c^{n-1}} I_{i,k}^{(n)} \right] \frac{\mu_0}{\mu}. \quad (24)$$

2.7. Planetshine

On the lit side of the rings seen at low phase, solar illumination is relatively bright so that any contribution from sunlight reflecting off the planet, or "planetshine," is comparatively negligible. However, this is not the case for the unilluminated side of the rings at low phase, or for either the illuminated or the unilluminated side of the rings at high phase. In these geometries, one cannot safely neglect planetshine.

2.7.1. Reflectivity Function

We begin by using the brightness data obtained by the *Pioneer 11* Imaging Photopolarimeter in the red (0.44 μm) and blue (0.64 μm) spectral regions on a single belt and a single zone of Saturn (Tomasko & Doose 1984), and the surface reflectivity models of these data, produced by Dones et al. (1993), using a Barkstrom law (Barkstrom 1973) for I/F:

$$\frac{I}{F} = \frac{A}{\mu_p} \left(\frac{\mu_p \mu_{p0}}{\mu_p + \mu_{p0}}\right)^B, \quad (25)$$

where μ_p and μ_{p0} are, respectively, the μ and μ_0 for the planet's surface. The empirically determined quantities A and B are functions of the phase angle and are taken from Table V of Dones et al. (1993).

We use this model in the same way as was done in Table V of Dones et al. (1993) except that in this case, the weighted average of the A and B values for the blue and red filters (assuming that each parameter varies linearly with wavelength) is different because the effective wavelengths of the Voyager clear filters are shorter than for the Cassini clear filters. The central wavelengths are 0.49 μm (Danielson et al. 1981) and 0.61 μm (Porco et al. 2004), respectively. Linear interpolation in the phase angle was used to determine the A and B values for phases between those tabulated in Dones et al. (1993).

To calculate the intensity of planetshine on the rings, a surface reflectivity function must be derived from Equation (25). The relationship, $I/F = \mu_{p0} \rho_s(\mu_p, \mu_{p0}, \alpha)$ (van de Hulst 1980), where $\rho_s(\mu_p, \mu_{p0}, \alpha)$ is the reflectivity, allows us to derive the surface reflectivity of the planet:

$$\rho_s(\mu_p, \mu_{p0}, \alpha) = \frac{A}{\mu_p \mu_{p0}} \left(\frac{\mu_p \mu_{p0}}{\mu_p + \mu_{p0}}\right)^B. \quad (26)$$

The intensity of light reflected from a point on the planet's surface is then given by

$$I = F \mu_p \mu_{p0} \rho_s(\mu_p, \mu_{p0}, \alpha), \quad (27)$$

where πF is the solar flux density on the planet.

2.7.2. Implementation

To implement planetshine, we gridded the planet into latitude and longitude intervals as shown in Figure 3. At each grid point and for any given geometry, we compute μ_p and μ_{p0}. If either of these is nonpositive (i.e., it is in shadow or out of view of the ring patch), the point is assigned an intensity of zero. We also trace the path from the Sun to the grid point and determine if the path first intersects the dense rings (A ring or B ring) at any point. If so, the point is in the rings' shadow and the intensity is set to zero. We do not yet accommodate the transparency of the A ring or the opacity of the C ring. If $\mu_p > 0$, $\mu_{p0} > 0$, and the point is not in the ring shadow, we proceed to compute the brightness from that point.

The intensity reflected from each surface element is proportional to its area:

$$\text{Area} = (\sin(\theta_2) - \sin(\theta_1)) \Delta\phi \, R^2, \quad (28)$$

where $\theta_2 > \theta_1$ are the latitudes of the element's boundaries, $\Delta\phi$ is its longitudinal width, and R is the planet's radius at the location of the element's center, which is variable over the body

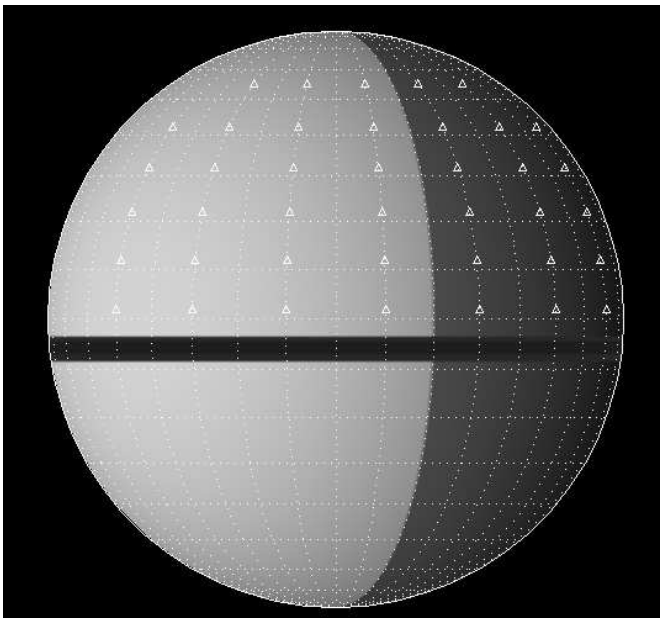

Figure 3. A sample calculation area of the planet's northern hemisphere used for planetshine in a patch of the A ring. An equivalent calculation is also done for the southern hemisphere to get the southerly component of planetshine. The dark band across the southern equatorial region is the shadow of the rings on the planet for a solar elevation angle appropriate for the Voyager epoch in the early 1980s.

owing to its oblateness. This formula is an approximation to the area of an element on an ellipsoid, but for small areas it is sufficiently accurate. Finally, the intensity of the light that reaches the ring patch is diminished as $1/d^2$, where d is the element-to-ring separation.

Rays with the calculated intensity (where we continue to define the solar intensity per ray as unity) are sent into the particle box from the direction of the center of the planet element. This is repeated for each illuminated element of the planet: that is, elements which reflect zero intensity are omitted.

From this point onward, the calculation of reflected/transmitted planetshine from the rings is the same as for sunshine.

3. RAY-TRACING EXPERIMENTS WITH RANDOM PARTICLE BOXES

To isolate the underlying vertical and horizontal physical ring structure (e.g., particle number density, vertical thickness, etc.) and particle properties (albedo and phase function), and the consequent scattering properties of the ring, we performed light-scattering experiments on boxes filled with particles randomly distributed in the box, with a dispersion in z provided by Gaussian deviates. The particles were given one of several possible phase functions. The Sun and observer positions and the optical depths and vertical thicknesses of the particle distributions were, in general, variable input parameters. All particle size distributions used in this section were unimodal, with 1 m radius particles.

3.1. Code Verification

We used random particle boxes to demonstrate the accuracy of the ray-tracing code by comparing our numerical results with those produced by the classical single-scattering radiative transfer solutions (Equations (16) and (17)), by the numerical results obtained by van de Hulst (1980), and by adding–doubling methods such as those used by Dones et al. (1993). van de Hulst computed I/F values for plane-parallel atmospheres of small, homogeneous, isotropic scatterers and tabulated the results for a variety of μ, μ_0, τ, and A. In the range of $1 \leqslant \tau \leqslant 32$, van de Hulst calculated intensities using the "doubling-and-adding" method, where the intensity from a slab of 2τ was determined based on calculations of the series of scatterings that occurs between two layers of optical depth τ.

Figure 4 shows a comparison among our light-scattering experiment, van de Hulst's (1980) tabulated results, and the classical single-scattering equations (Equations (16) and (17)).

The agreement between our light-scattering experiments and van de Hulst's (1980) results is good: the maximum deviation

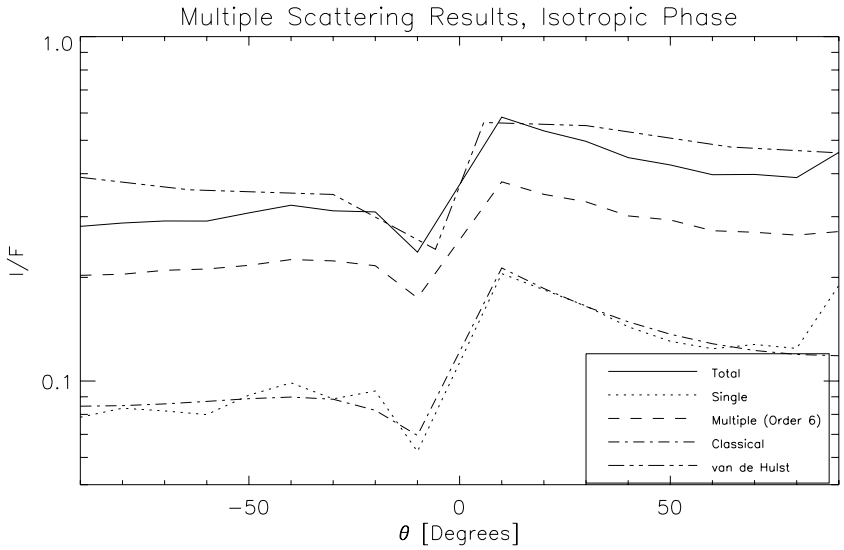

Figure 4. Comparison among our numerical results, van de Hulst's (1980) tabulated results (which include multiple scattering), and classical analytical (i.e., single-scattering) results for a classical multiparticle-thick ring. The box in this experiment had 5000 particles, each of which had a radius of 1 m. Particles were randomly distributed in the horizontal dimension, with a Gaussian distribution in the vertical dimension with $\sigma_z = 30$ m, that is, thick enough to resemble a classical ring. The particle distribution had a dynamical optical depth of $\tau_d = 1.47$, a physical optical depth $\tau_p \sim 2$, and the particles had an isotropic phase function and an albedo $A = 1$. Solar illumination is directly from above. These particle and illumination characteristics match those used by van de Hulst (1980). The total I/F in this figure is the sum of our single-scattering and multiple-scattering runs (which go out to sixth order), and matches van de Hulst's results well.

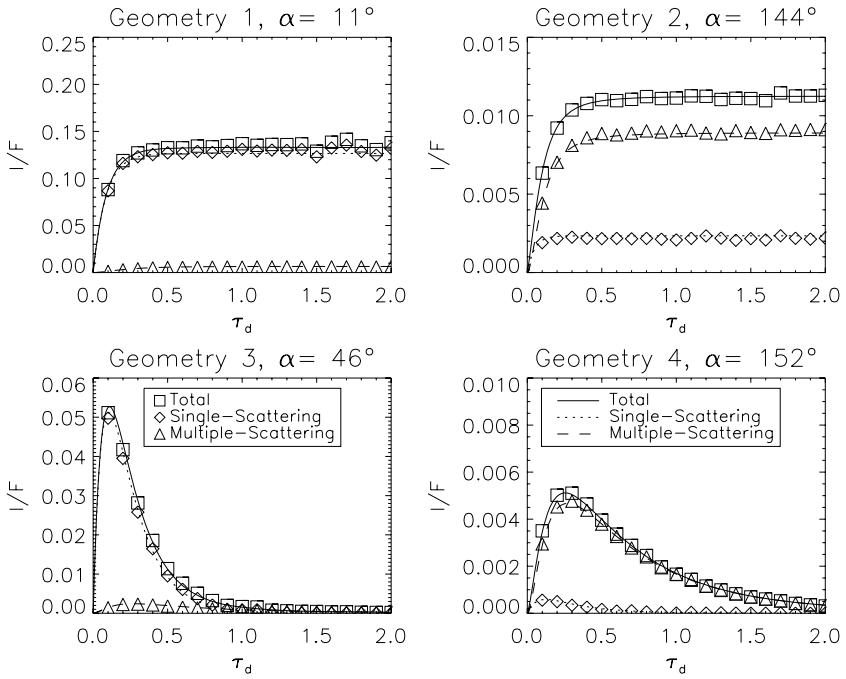

Figure 5. Comparison of I/Fs from the ray-tracing code (symbols) and adding–doubling (solid, dotted, and dashed lines) using the Lambert phase function for four different geometries. Upper plots are lit face; lower plots are unlit face. The geometries approximately correspond to Voyager images: Geometry 1—FDS 43916.56 ($\theta_0 = 8.^\circ0$, $\theta = 12.^\circ7$, $\alpha = 11^\circ$), geometry 2—FDS 34953.57 ($\theta_0 = 3.^\circ9$, $\theta = 9.^\circ7$, $\alpha = 144^\circ$), geometry 3—FDS 34934.57 ($\theta_0 = 3.^\circ9$, $\theta = -10.^\circ5$, $\alpha = 46^\circ$), and geometry 4—FDS 34947.01 ($\theta_0 = 3.^\circ9$, $\theta = -15.^\circ8$, $\alpha = 152^\circ$), respectively.

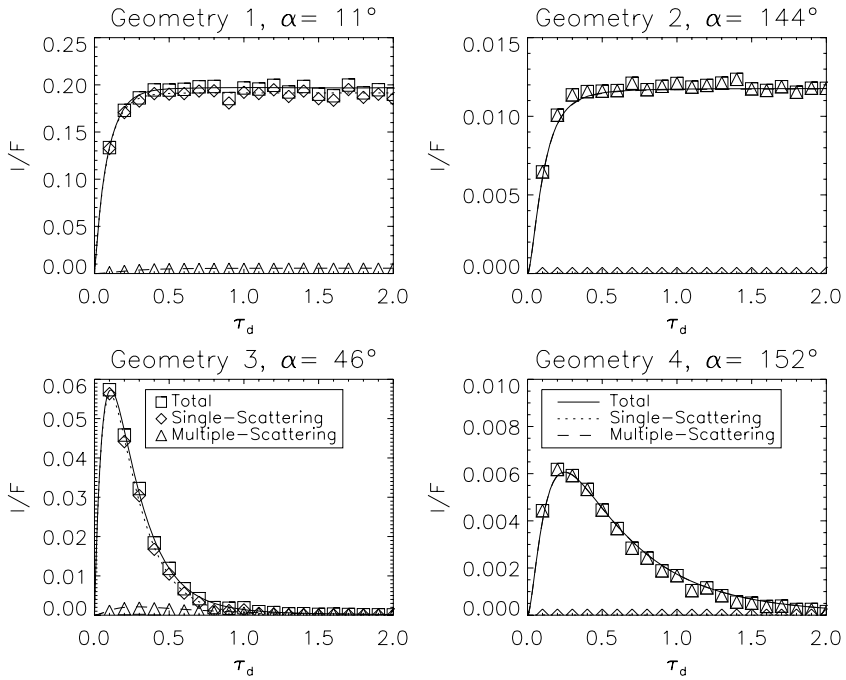

Figure 6. Same as Figure 5, but using the Callisto phase function rather than the Lambert phase function.

anywhere in Figure 4 between the two sets of results is of order 20%. The assumptions inherent in this comparison—that is, the normal incidence of the Sun, the unity albedo of the particles, and the isotropic phase function—significantly enhance the importance of multiple scattering compared with real observations in which the Sun is never more than 27° above Saturn's ring plane. The discrepancy, therefore, is likely due to an inadequate number of orders of multiple scattering in these ray-tracing experiments. In realistic cases, the discrepancies will be much smaller.

A similar test is shown in Figure 5. We compare the results of an adding–doubling code with those obtained with our ray-tracing code for four geometries from the Voyager encounters: low- and high-phase viewing of the lit and unlit sides of the rings, respectively. Both methods employ the Lambert phase function. The two methods give virtually identical results up to the noise level in the ray-tracing curves. This agreement validates both the ray-tracing method and the implementation of the Lambert phase function. As a further check, in Figure 6, we show the results of the same test, with the Lambert function

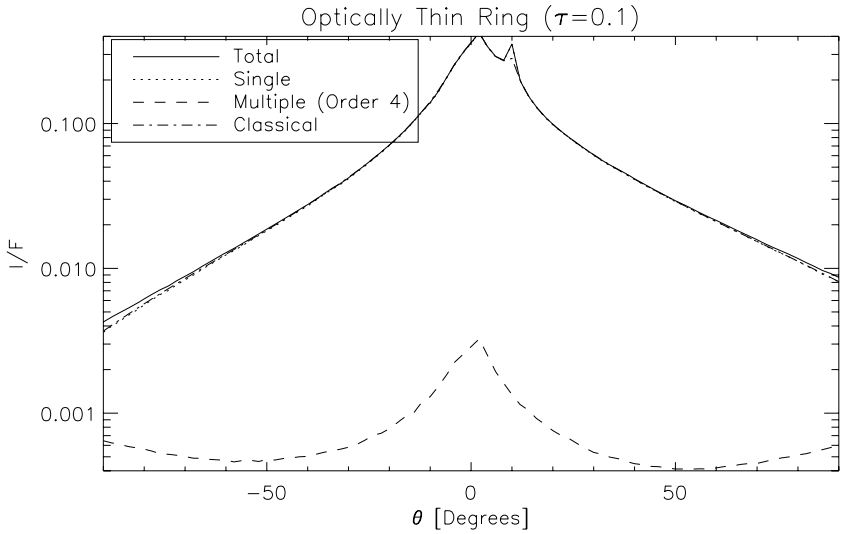

Figure 7. Brightness scan from the lit side to the unlit side of an optically thin ring with $\tau = 0.1$ and $\sigma_z = 80$ m. The Sun is at $\theta_0 = 10^\circ$ above the ring plane. The observer moves from $\theta = -90^\circ$ to $\theta = 90^\circ$. The ring is predominantly seen in single scattering; even when the observer is within 5° of the ring plane, multiple scattering is small.

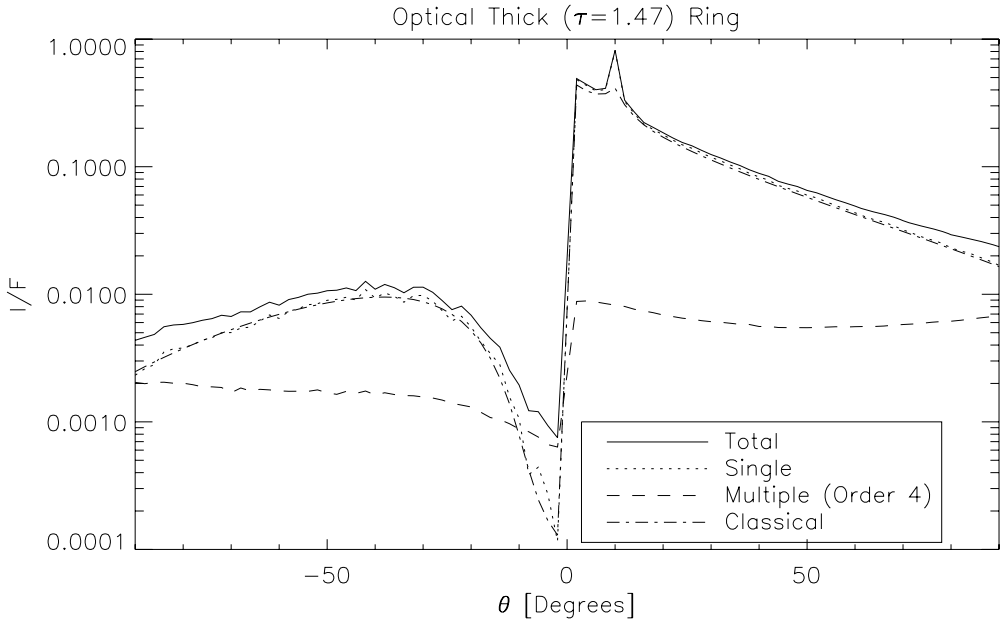

Figure 8. Same as Figure 7, but for an optically thick ring, $\tau = 1.47$, $\sigma_z = 160$ m. The ring is seen predominantly in single scattering except in a narrow elevation range from 0° to ∼−10°. Because of the ring's optical thickness, however, multiple scattering becomes a substantial component of the ring's unlit side brightness.

replaced by the Callisto function. We again find good agreement between the adding–doubling and ray-tracing results, validating the implementation of the Callisto phase function.

Figure 7 illustrates another experiment: the change in brightness with the observer viewing angle of an optically thin ring with $\tau = 0.1$, $\sigma_z = 80$ m. The particle radii were all 1 m. This is a classical, multiparticle-thick box, in which the particles are well separated. The observer moves from $\theta = 90^\circ$ to $\theta = -90^\circ$. The ring is predominantly seen in single scattering; even within 5° of the ring plane, multiple scattering is small. The opposition effect (caused by mutual particle shadowing) is not prominent in the case of an optically thin ring; the I/F here grows as the observer passes through the ring plane because of the increase in the slant optical depth through the optically thin ring. Our ray-tracing code reproduces the analytic single-scattering results.

Figure 8 illustrates the same variation of the observer emission angle but for an optically thick ring, $\tau = 1.47$, $\sigma_z = 160$ m. The ring is predominantly seen in single scattering. Because of the ring's optical thickness, however, multiple scattering becomes a substantial component to the total brightness of the ring's unlit side. The analytic single-scattering equation (Equation (17)) underestimates the ring's unlit-side brightness by up to a factor of ten in some geometries.

To verify the implementation of the planetshine portion of the code, we have compared our results with those generated by the same adding–doubling code used in Dones et al. (1993). Figure 9 compares the planetshine results for two different illuminated face geometries: one at low phase and the other at high phase. For both geometries, the two codes give identical results, validating the implementation of the planetshine model.

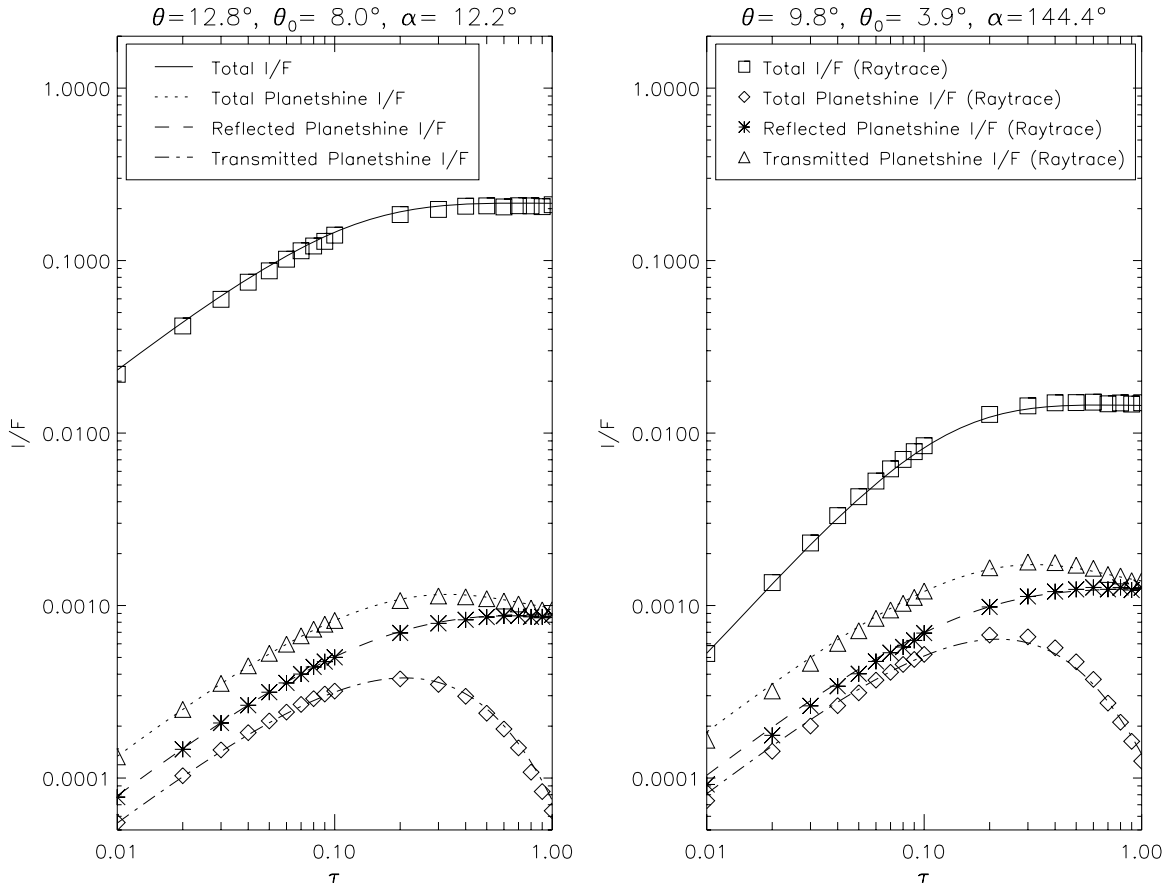

Figure 9. A comparison of planetshine computed using an adding–doubling code (Dones et al. 1993) and the ray-tracing code. The geometries are similar to those of Voyager images FDS 43916.56 and FDS 34953.57 (see Figure 5). Lines show the adding/doubling results and the symbols show our results. Plot titles indicate the solar and observer elevations (θ_0 and θ) and the phase angle α.

3.2. Variation of Ring Brightness with Ring Parameters and Geometry

3.2.1. General Geometries

To investigate the dependence of a ring's brightness on vertical thickness, optical depth, and viewing and illumination geometry, we have conducted a study of the variation of the ring reflectivity versus optical depth, solar illumination angle, and emission angle (including lit and unlit geometries) for a variety of random particle boxes, both thick and thin. Sixteen random particle boxes were created in which the thickness of the vertical distribution was specified by $\sigma_z = 2$, 4, 8, and 16 m, and the optical depth was taken to be $\tau = 0.05$, 0.1, 0.5, and 1.0, respectively. The number of particles was 5000. The particles were given a radius $r = 1$ m, an albedo $A = 1.0$, and a Callisto phase function. In all cases, the difference in azimuth between the observer and the Sun is 20°; this provides enough separation to avoid the opposition effect except possibly at the smallest values of σ_z (see Section 3.2.2). Classical single-scattering calculations were made for the stated geometry and optical depths.

We begin with an examination of *low-phase* geometries. The results are shown in Figures 10–12.

In Figure 10, we compare for $\tau = 0.5$ (comparable to that in Saturn's A ring) the variation of the I/F with the emission angle (or, equivalently, elevation angle) for two different solar incidence angles: 80° (i.e., 10° above the ring plane) and a more penetrating 60° (or 30° above the ring plane). At all elevation angles, the more penetrating the sunlight (i.e., the lower the incidence angle), the brighter the ring, regardless of vertical thickness.

In Figure 11, we kept the solar incidence angle constant at 80° (or a solar elevation angle of 10°) and grouped the lit face viewing results according to the optical depth of the box. In Figure 12, we did the same for the unlit face viewing geometry.

Our results reproduce, or asymptotically approach, those of the classical calculation for thick boxes, regardless of the optical depth, illumination angle, or emission angle (either lit or unlit side), giving us confidence in its accuracy. Not surprisingly, we find that optically thick ($\tau = 0.5$ and $\tau = 1.0$) boxes are inherently brighter than optically thin boxes in the lit-face geometry; for the unlit-face geometry, as the optical depth increases from a low value, the brightness increases at first and then decreases when the optical depth becomes large enough to impede diffuse transmission through the ring. All boxes viewed on the lit side grow brighter as the observer's view grows more oblique (i.e., toward a lower elevation angle). This is true even for optically thinner boxes, although the optically thicker boxes undergo more dramatic changes in reflectivity with a decreasing elevation angle. Also, the most dramatic change occurs for a more penetrating illumination angle on a thin ring ($i = 60°$ versus $i = 80°$) since in this geometry there is less shadowing and a more illuminated particle area to see. On the unlit, as on the lit, side, the rings grow brighter with more oblique viewing geometries, *except* for optically thick rings for which a point is reached where, after growing in brightness, the rings grow dimmer with more oblique viewing.

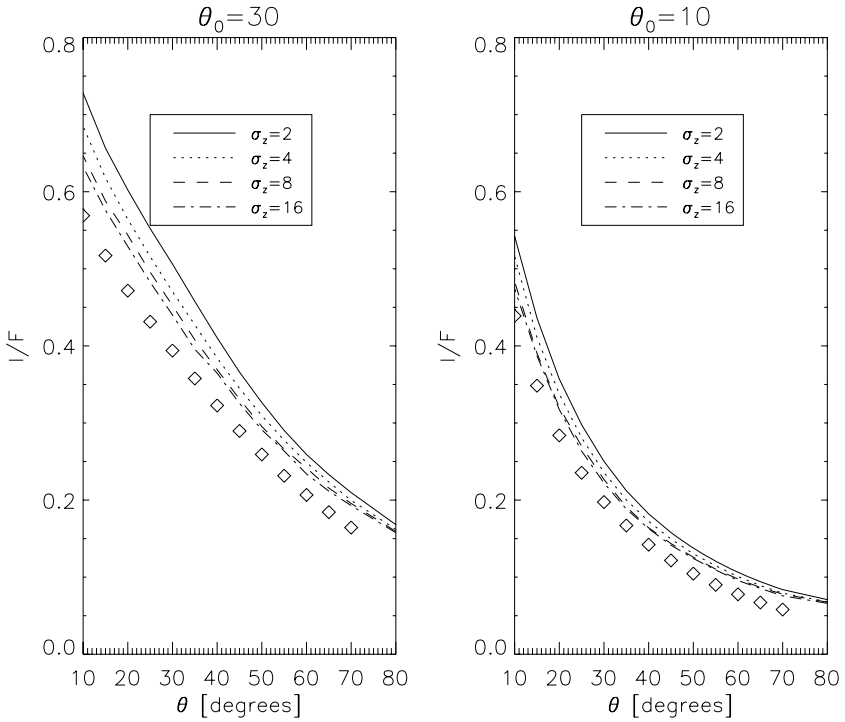

Figure 10. Light-scattering experiments performed over a variety of lighting and viewing conditions, on a set of four boxes with optical depth $\tau = 0.5$ and with varying vertical thickness: from relatively thick $\sigma_z = 16$ to thin $\sigma_z = 2$. The diamonds are classical single-scattering calculations (Equation (16)) for a many-particle-thick ring. The solar incidence angle is changed from one panel to the next. In all cases, the albedo is 1 and the observer longitude is 20°.

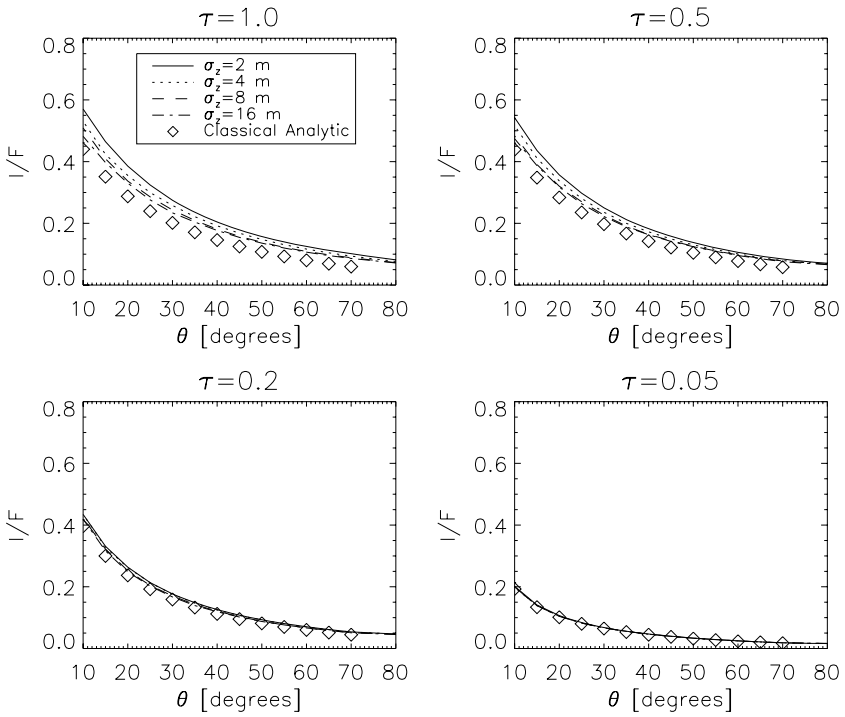

Figure 11. Ring brightness (I/F) as a function of the observer elevation angle, θ, in simulations with boxes of $\sigma_z = 2, \ldots, 16$ m and lit-face, low-phase viewing. Different panels show different optical depths. The difference in longitude of the source and observer is $\Delta\lambda = 20°$. The solar elevation angle was kept constant at $\theta_0 = 10°$. Classical single-scattering calculations (Equation (16)) are shown as diamonds. In all cases, the albedo is 1 and the observer longitude is $\lambda = 20°$.

To illustrate more clearly how the brightness of rings of different optical depths might vary in an image of Saturn's rings (at a single illumination and viewing geometry), in Figure 13 we group the lit face, low-phase results for four discrete emission angles, as a function of optical depth.

In Figure 14, we compare the differences in light-scattering behavior between low and high phases for different optical depths. As in previous experiments shown in Figures 9 through 13, random particle boxes were used. But the particles in this case have albedos and phase functions appropriate for a

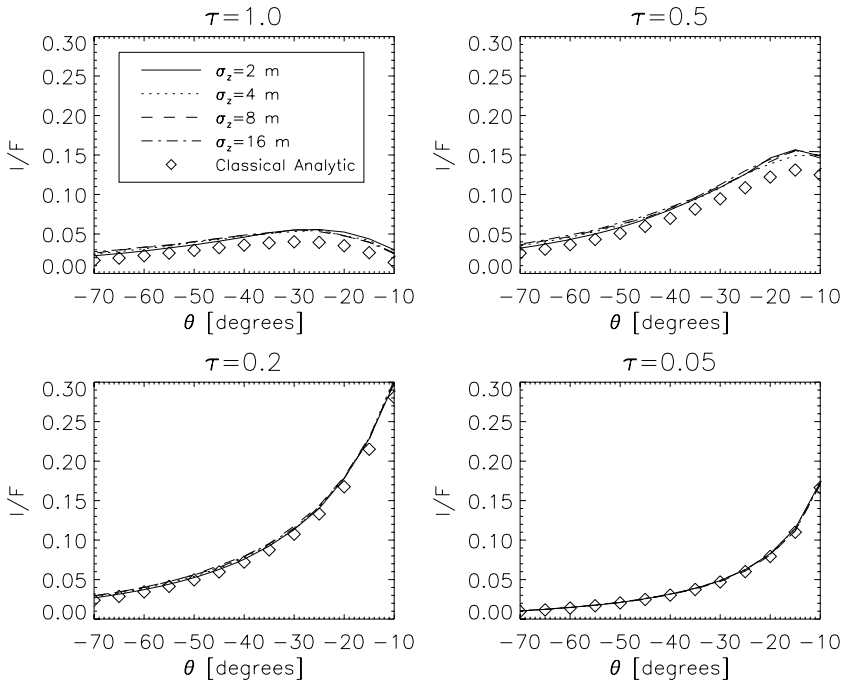

Figure 12. Same parameters as in Figure 11, except now for the unlit side at low phase angles. The albedo is 1 and the observer longitude is 20°. The diamonds are classical single-scattering calculations (Equation (17)) for a many-particle-thick ring.

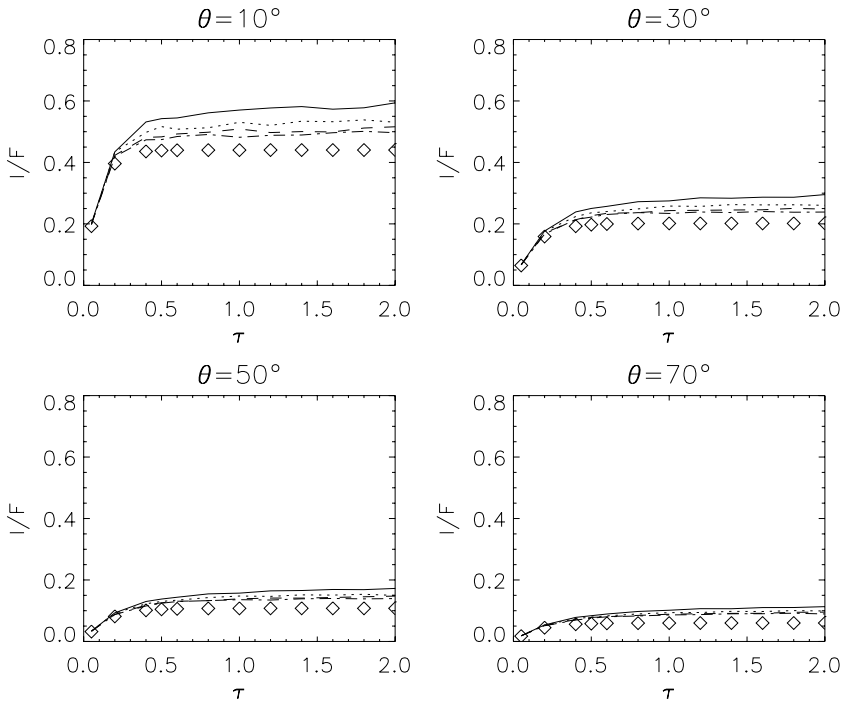

Figure 13. Data from Figure 11, now plotted to show the variation of simulated I/F vs. optical depth for boxes of varying thicknesses. Different panels show different observer elevation angles. In all cases, the albedo is 1, the solar elevation is 10°, and the observer longitude is 20°.

particular region of Saturn's rings as observed in Cassini images. We plotted these ray-tracing results for boxes of varying optical thicknesses and geometries specific to two Cassini images: one low (37°) and the other high (146°) phase. Different curves denote boxes of different thicknesses.

Examination of Figure 11 and the left (low phase) and right (high phase) plots in Figure 14 is very provocative. We find that (1) while optically thick rings are brighter than optically thin rings, regardless of phase, the physical thickness of a ring will determine its brightness at nonzero emission angles, and that the relationship between physical thickness and brightness reverses sign between low and high phases; (2) the relationship is such that the rings, when viewed at high phase (where multiple scattering dominates for backscattering particles) get *dimmer* as the ring gets physically thinner, regardless of τ, in contrast to the behavior at low phase. This is clearly because of reduced opportunity for multiple scattering in physically thin rings; (3) the brightness of physically thin rings changes most dramatically

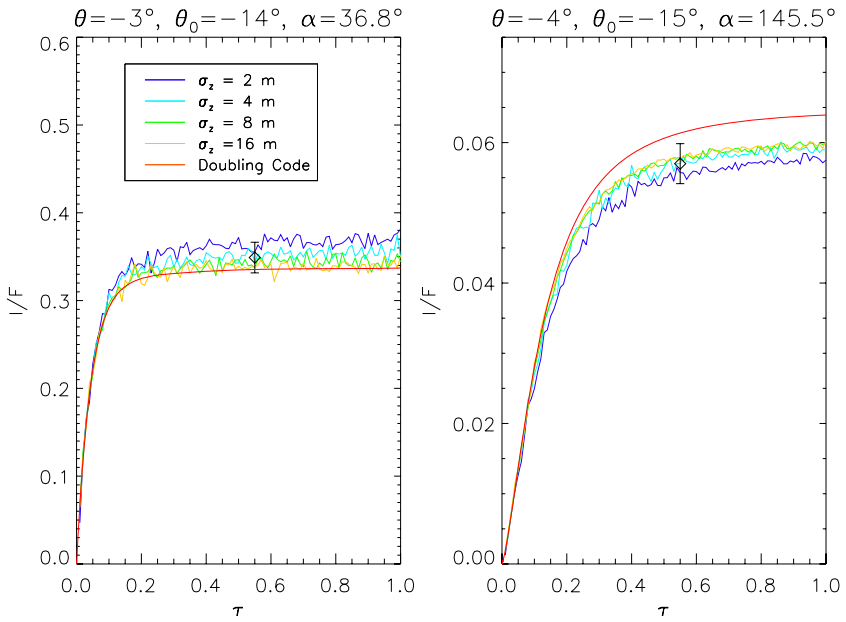

Figure 14. Models of I/F vs. optical depth in the A ring exterior to the Encke gap (orbital radius: 135,000 km) for a low-phase (left) and a high-phase (right) geometry. Rings with random particle locations were used, and different curves denote different vertical ring thicknesses in the models. The solar and observer elevation angles are given above each plot, as well as the phase angles. Data points (diamonds) were taken from Cassini images having the same geometries as the models. (The optical depths of the data are physical optical depths and, because they are less than 1, are equivalent to the dynamical optical depth which is plotted here.) Multiple scattering up to third order was calculated in the ray-tracing models. Albedos and phase functions were adjusted until the model curves with the same thickness passed through the data points in both plots. (See text for additional constraints.) The resulting values were an albedo = 0.63 and a power-law phase function with an index of 2.624. Data are from Cassini images N1547753879 and N1521540684.

in the optical depth range from about $\tau = 0.1$ to $\tau = 0.4$ or so, and then more or less levels out as τ grows. However, the greatest growth in reflectivity of thin rings beyond $\tau \sim 0.4$ occurs for the most oblique viewing angles.

We also compare our model results to Cassini observations in Figure 14. To this end, measurements of brightness were made on two Cassini images of the outer A ring: one taken at low (37°) and the other high (146°) phase. The portion of the A ring exterior to the Encke gap has been shown to display only a weak azimuthal asymmetry (Dones et al. 1993; Colwell et al. 2006; French et al. 2007a), suggesting that self-gravity wakes are not very prominent. Hence, ray tracing of random particle boxes is appropriate for modeling this region.

The images were first calibrated using the standard Cassini Imaging Science Subsystem (ISS) calibration pipeline that has been coded in the CISSCAL software package (Porco et al. 2004). The diamonds in Figure 14 show the resulting measurements of I/F, with the 5% uncertainty in the calibration of the images. The true normal optical depth of the region ($\tau = 0.55$) was derived from Cassini Ultraviolet Imaging Spectrograph (UVIS) stellar occultation data (Colwell et al. 2006). The ray-tracing model curves that are shown were calculated by requiring that the data points lie, for both low- and high-phase geometries, on the curves having identical thicknesses. The resulting best-fit phase function is a power law based on Dones et al. (1993) with an index of 2.624; the best-fit albedo is $A = 0.63 \pm 0.03$. This albedo and phase function are consistent with that inferred from photometric measurements made during Cassini's approach to Saturn (Porco et al. 2005). The nominal ring thickness we find is ∼4 m thick (standard deviation) or about 10 m thick FWHM, in agreement with values of ring thickness estimated for other regions in the A ring from Cassini stellar occultation data (Colwell et al. 2006; Hedman et al. 2007), though the calibration uncertainties in the data make an exact assignment of ring thickness difficult. Continued refinements in the calibration of Cassini images will hopefully improve this situation. However, at the moment the high phase observations and models—the ones with the greatest sensitivity to ring thickness—suggest an A ring thickness that is not a classical "multiparticle thick" ring.

It may at first be surprising that we find photometric properties for a thin ring that agree with values obtained using an adding/doubling technique (Porco et al. 2005) that assumes a classically "thick" ring. The reason is that at the intermediate phase angles (∼66°) of the images analyzed in Porco et al. (2005), the brightness of the ring was insensitive to ring thickness. Hence, it is assuring that we find the same values of the phase function and albedo for other (i.e., low- and high-phase) geometries as we found in Porco et al. (2005).

The same approach can be applied to the C ring, where self-gravity wakes also appear to be absent (Dones et al. 1993; French et al. 2007a). In Figure 15, we show the results of an analysis similar to that done in the A ring, except that here we have included a medium-phase geometry as well and we have applied an additional constraint to derive the particle properties. We have required that the "best-fit" phase function and albedo also reproduce the brightness and form of planetshine reflected from the C ring (see Section 3.3). Brightness measurements were taken from three Cassini images of the C ring in a region where the optical depth is 0.09 based on measurements from stellar occultations observed by the Voyager PPS and Cassini UVIS instruments (J. Colwell 2007, private communication), which agree well with each other. Our best fit yields a power-law phase function with an index of 3.092, within the range (between 3 and 4) found by Cooke (1991) using Voyager data. This phase function is close to the Callisto phase function (Figure 1). The ring particle albedo is $A = 0.32 \pm 0.02$, notably lower than the albedos measured in the A and B rings, and agrees with that

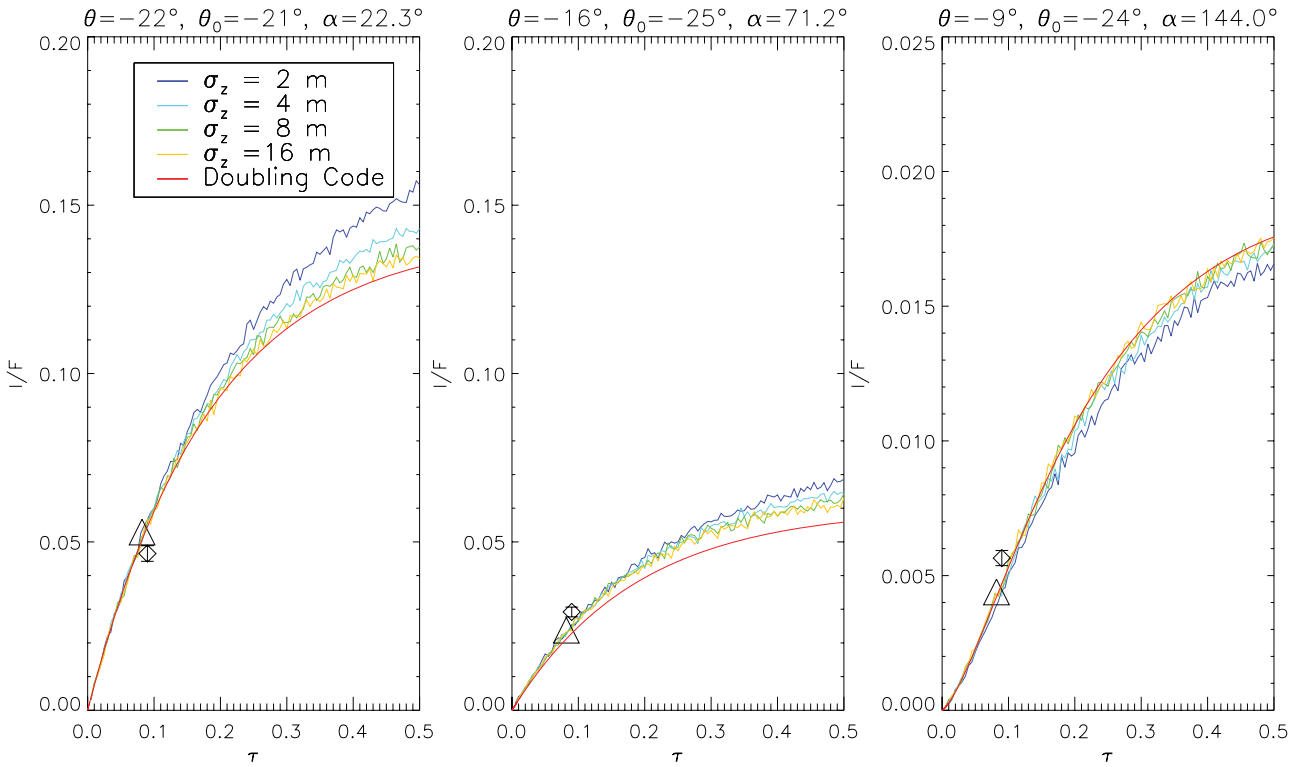

Figure 15. Models of I/F vs. optical depth in the C ring (orbital radius: 85,300 km) for a low-phase (left), a medium-phase (middle), and a high-phase (right) geometry. Because of the low albedo of particles in the C ring, we only needed to calculate two orders of scattering in the ray-tracing models. Plots are similar to Figure 14. A power-law phase function with an index of 3.092 (close to a Callisto phase function; see Figure 1) and an albedo of 0.32 gave the best results. See text for details. Data are from Cassini images N1477742794, N1464246905, and N1477743777. Triangles show ray-tracing runs on random boxes containing particles with a size distribution found in (French & Nicholson 2000): $r_{\min} = 0.01$ m, $r_{\max} = 10.0$ m, and $q = 3.1$. These test cases showed no difference from the unimodal model curves, suggesting that we do not need to use the size distribution for this experiment.

found in earlier work (Porco et al. 2005) from adding–doubling methods.

Unfortunately, the low optical depth in the C ring puts it on the portion of the curve that is insensitive to ring thickness.

3.2.2. Opposition Surge Geometry

The opposition surge is a well-known phenomenon that is nearly ubiquitous in light-scattering situations near exact backscatter, such as looking at the halo around one's own shadow when it falls on a rough surface. Photographs taken by the Apollo astronauts of their own shadows show this effect. Most airless bodies in the Solar System show an opposition effect, and Saturn's rings (where the effect was first discovered in the nineteenth century) are no exception. The opposition effect has been recently seen in Cassini data taken with the Visible and Infrared Mapping Spectrometer (VIMS; Nelson et al. 2006; Hapke et al. 2006) and ISS (Déau et al. 2006) instruments. This effect is distinct from the gradual rise in brightness of a single body toward zero phase that arises from seeing more of the illuminated surface of the body as the phase angle decreases.

Explanations for the opposition effect on Solar System bodies fall into three broad categories. First, intraparticle shadowing explains the effect with surface roughness on scales ranging from the sizes of grains within the regolith that covers a ring particle to that comparable to the particle itself. At exactly $\alpha = 0°$, the entire visible surface is lit directly, and no shadows are visible to the observer. As the observer separates from the source and α increases, the observer sees more and more of the shadows caused by surface roughness. It is generally believed that while intraparticle shadowing plays a role in determining the shape of the phase curve in backscatter, it cannot produce the narrow opposition surges, with widths of a few degrees or less, that are seen on many small bodies.

Second, interparticle shadowing occurs when particles that are not in physical contact shadow each other. Interparticle shadowing is the traditional explanation for the opposition surge of Saturn's rings (Irvine 1966). Again, at $\alpha = 0°$, the observer is looking only at the illuminated sides of ring particles, and the rings appear brighter than they do at larger phase angles, at which the observer can see the shadowed portions of the particles and the brightness decreases. The width and depth of the opposition surge depend on the size distribution and spatial distribution of particles in a ring: both a physically thicker ring and a broader size distribution lead to a narrower surge. A strong surge due to interparticle shadowing can only occur along paths with sufficient optical depth to allow mutual shadowing: that is, $\tau_p/\mu \gtrsim 1$.

Third, a physical optics effect known as coherent backscattering likely contributes to the rings' opposition surge (Mishchenko & Dlugach 1992). This process involves multiple scattering between microscopic grains within the regolith. Of the three mechanisms, coherent backscattering generally produces the narrowest brightness surge. Recent observations by *HST* and the Cassini cameras indicate that the rings' surge has a half-width at half-maximum of only 0°.1–0°.3 and an amplitude of 1.4–1.6, where we define the amplitude as the actual I/F at the zero-phase angle divided by the extrapolated I/F derived from measurements at low phase angles (French et al. 2007b;

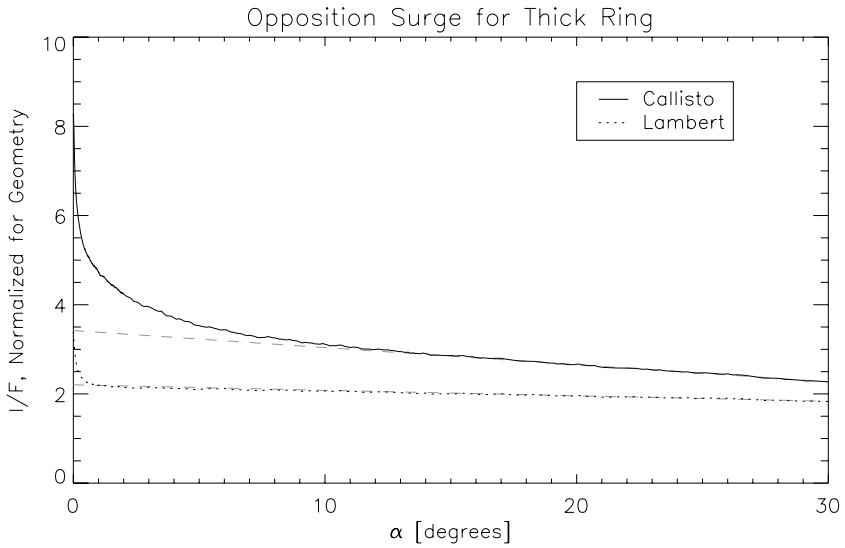

Figure 16. The opposition surge for a ring with a very large thickness of $\sigma_z = 160$ m. The Lambert phase function shows a surge peak of amplitude 1.4 times the background and with a half-width at half-maximum of 0.°1. The Callisto peak has amplitude 2.5 times the background and a half-width at half-maximum of 0.°2. The Lambert function has a narrower peak in this case because its surge is almost entirely due to interparticle shadowing, an effect that only becomes pronounced, and very low phase angles. The Callisto phase function has a built-in surge which is wider than this, so it shows a broader peak here. (The background level is defined as the value of I/F at exactly 0° phase that is determined by extrapolating to 0° the phase curve beyond ∼10°, as indicated by the dashed line.)

Déau et al. 2008). The angular width of the surge is narrower than that found by previous lower-resolution Earth-based studies (e.g., Franklin & Cook 1965), which did not get as close to zero phase as recent observations. Furthermore, Lyot (1929) observed the surge in brightness to correlate with a decrease in the polarization fraction, as a function of the phase angle, having the same shape, suggesting a similar cause for both. Such a surge is expected for coherent backscattering, which our ray-tracing code cannot model.

The rings' brightening at phase angles less than ∼10° is presumably a combination of coherent backscattering and interparticle shadowing. We have performed several simulations of the opposition effect using both Lambertian and Callisto phase functions. The Callisto phase function, based as it is on a real planetary surface, already has a modest built-in opposition surge (Squyres & Veverka 1981). The ring particles are likely to have icy compositions similar to Callisto's surface, although their surfaces may be more evolved than those of Callisto due to their collisional environment. In any case, our results suggest that a Callisto-like phase function applies to the low optical depth portion of the C ring.

The ray-tracing simulations of the opposition surge, using 1 m particles with Lambert and Callisto phase functions, and a vertical ring thickness of $\sigma_z = 160$ m, are shown in Figure 16. The Lambert opposition surge has a half-width at half-maximum brightness of 0.°1 and an amplitude of ∼1.4. Because of the nature of the Lambert phase function, which pertains to an idealized perfectly diffusing surface, the surge shown here (above and beyond the usual upturn toward low phase in any physically realistic phase curve due to the increasing visibility of the illuminated surface toward zero phase) is entirely due to mutual shadowing by particles.

The opposition surge model using the Callisto phase function has a half-width at half maximum brightness of 0.°2 and an amplitude of ∼2.5. Because this phase function has its own opposition surge, the curve consequently accounts for both shadowing on the surface (intraparticle) and shadowing between bodies (interparticle).

The opposition surge is dependent on the thickness of the ring. Consider, for example, the limiting case of a monolayer of particles. In this case, mutual shadowing will be only a minor effect for most illumination and observation geometries, reducing the magnitude of the surge. To characterize the variations in the opposition surge with ring thickness, we have produced additional surge curves for a ring thickness of $\sigma_z = 2$ m, shown in Figure 17. For this ring, the Lambert particles show a half-width of 3° and a surge amplitude of ∼1.3. For the Callisto-surface particles, the half-width is 2° and the amplitude is ∼1.9.

It is apparent that the main effect of thinner rings is to broaden the opposition surge. This is a well-known result (see, e.g., Irvine 1966). The heights of the surges are only slightly affected, lowering them by about 20%. The Cassini ISS experiment has acquired (and continues to acquire) images of the rings that include the opposition surge, the purpose of which is to eventually produce an estimate of the thickness of the rings using this phenomenon. In the future, we will compare our simulations with Cassini observations of the rings' opposition surge (Déau et al. 2008).

3.3. Comparison of Planetshine Models to Data

Many Cassini images taken at either high phase or of the unilluminated side of the rings show strong azimuthal variability in the A, B, and C rings. Since these images roughly show the same azimuthal dependence in all three rings, it is unlikely that the effect is due to canted structures in the rings like the wakes discussed above, particularly as the background C ring is believed to be devoid of them. However, the variations are quite consistent with what is expected from planetshine.

The A ring (and very likely the B ring) contains dynamical structures (Colwell et al. 2007; French et al. 2007a), that produce asymmetric brightness variations with longitude that complicate any attempt to model the azimuthal variation of reflected/transmitted planetshine on the rings. The C ring plateaus are similarly rich with small-scale (∼10 km) aggregate structures (J. Spitale 2007, private communication) and may

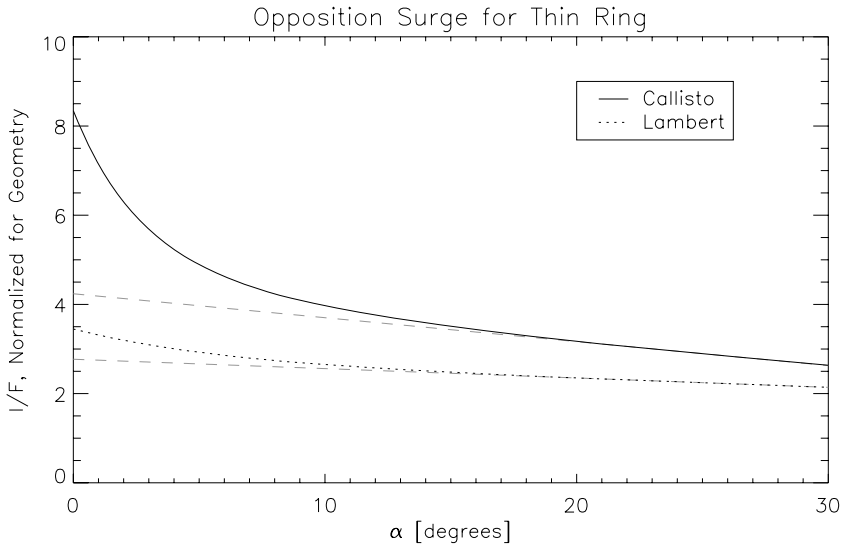

Figure 17. The opposition surge for a ring with $\sigma_z = 2$ m. The Lambert phase function shows a surge peak of amplitude 1.3 times the background and with a half-width at half-maximum of 3°. The Callisto peak has amplitude 1.9 times the background and a half-width at half-maximum of 2.°0. (The background level is defined as the value of I/F at exactly 0° phase that is determined by extrapolating to 0° the phase curve beyond ∼20°, as indicated by the dashed line.)

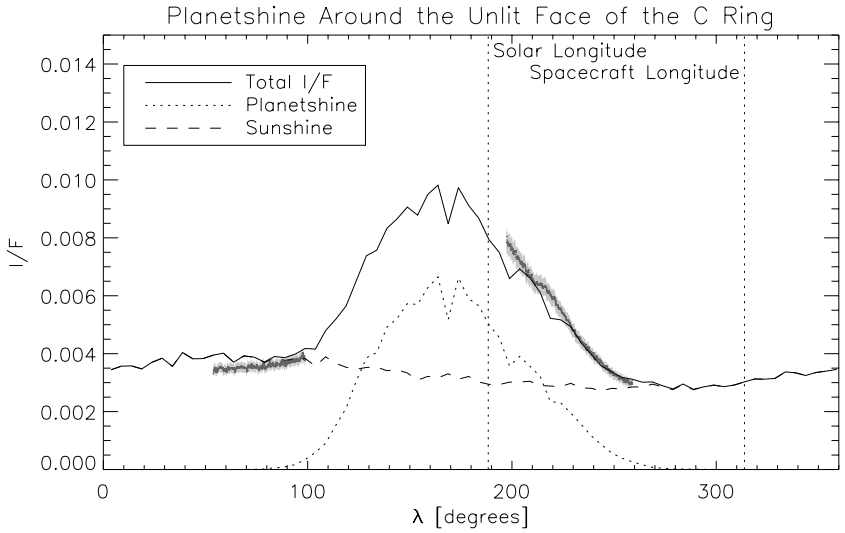

Figure 18. Data and model of reflected planetshine for the unlit face of the C ring. The model is shown in black lines while the measurements are the gray points. The light gray regions are error estimates for the data calibration. The solid line is the total I/F for the model, the dotted line is the planetshine contribution, and the dashed line is the directly scattered sunshine contribution. The orbital radius of the scan is 85,300 km, placing the region away from any C ring plateaus. The longitudes of the Sun and spacecraft are indicated with vertical dotted lines. Data are taken from Cassini images W1532506579 and W1532582920 (with $\theta_0 = -17°$, $\theta + 15°$, $\alpha \approx 128°$, and skyplane resolution = 62 km/pixel).

present a similar problem, so they are also a nonideal place to start our study of planetshine. Hence, the best starting point for comparison of planetshine data and models is in the background C ring, away from the plateau regions, where the optical depth is ∼0.1.

Accordingly, azimuthal scans were made in Cassini clear-filter images taken at a phase angle on the rings of ∼90°, at an orbital radius of 85,300 km, away from any plateaus. The two images used for the scans were taken within a very short time of each other so that the observation geometry is nearly identical for both ansae of the ring.

To model this part of the C ring, we use as before a random particle box. However, in this case, we used particles ranging in size from 1 cm to 10 m with an index of 3.1, consistent with French & Nicholson (2000), and an optical depth of 0.09. The particles were distributed uniformly in x and y and with a Gaussian distribution in z. Since the brightness of a low optical depth ring is insensitive to ring thickness (Figure 11), we have arbitrarily chosen the vertical thickness to be $\sigma_z = 11$ m.

Figure 18 shows the model (dark black curves) and data (gray points) for images on the unlit side of the rings. The solid black line shows the total model I/F, the dashed line displays the contribution from the directly scattered sunshine, and the dotted line shows the contribution from scattered planetshine.

The particle albedo and phase function that give the best match between the planetshine model and the data's overall intensity, as well as yield the best match between the scattered-sunlight models and the data presented in Figure 14, are the same values found for the C ring as imaged through the Cassini red filter (Figure 15), which is nearly identical in effective wavelength ($\lambda_{\rm eff} = 0.65$ μm) to the clear filter we are using

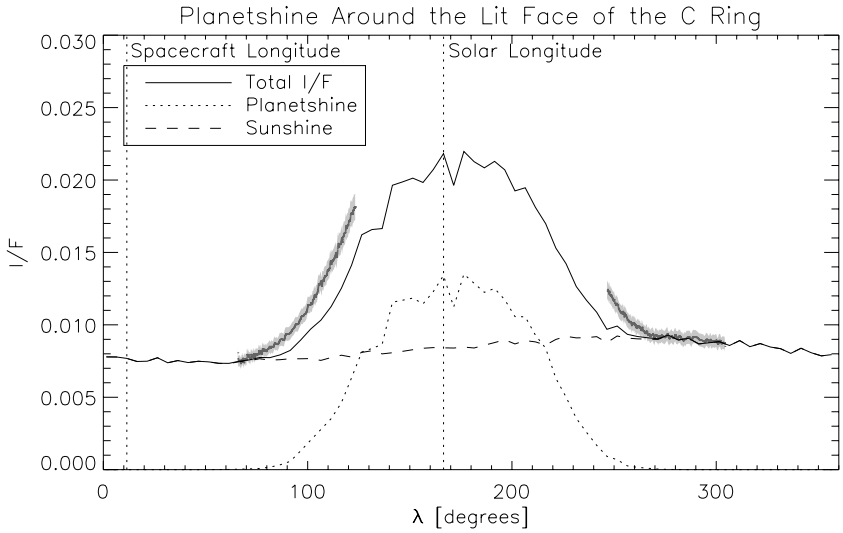

Figure 19. Data and model of planetshine for the lit face of the C ring. Vertical lines have the same meaning as in Figure 18. The scan is taken at an orbital radius of 85,300 km. Data are from Cassini images W1481837365 and W1481839829 (both with $\theta_0 = -23°$, $\theta \approx -4°$, $\alpha \approx 148°$, and skyplane resolution = 37 km/pixel).

here (Porco et al. 2004). These values are $A = 0.32 \pm 0.02$ and a Callisto-like power-law phase function with index = 3.092.

Another notable result of the model presented in Figure 18 is that it shows an I/F peak with a location and a morphology consistent with the data. The location of the peak is set by two things: the phase function of the planet and the phase function of the particles. The former determines the longitudinal variation in the intensity of illumination from the planet falling on the ring. If only the planetshine illumination mattered (i.e., if the particles had an isotropic phase function), then the peak intensity in planetshine would be at the subsolar longitude. However, the particles' phase function determines how much of the planet's light makes it to the observer from a ring patch in a given viewing geometry. All realistic phase functions for ring particles are backscattering, even those that do not have built-in opposition surges (such at the Lambert phase function). Thus, the particles' phase function tends to drive the planetshine peak to the antispacecraft longitude. The observed peak should lie somewhere between the subsolar and antispacecraft longitudes.

The data and models put the peak in the expected location: the subsolar longitude is indicated in Figure 18 and the antispacecraft longitude is at 130°. The planetshine peak lies between those bounds but is closer to the antispacecraft longitude, suggesting that the particles' phase function is the dominant effect. However, it is clear that both effects are important since the actual peak is clearly somewhere between the bounding longitudes.

The scan of the unlit C ring can be compared to Figure 19, a scan of the lit side of the C ring. (Note that the subsolar and subspacecraft longitudes have changed from where they were during the unlit side observation.) The obvious difference between the lit and unlit side observations is that, in the former, the I/F is higher everywhere. This is entirely to be expected since, in the former, the sunlight is not attenuated by passage through the rings, and the planetshine is more intense on the hemisphere with the subsolar point. The planetshine peak is still located between the subsolar longitude and the antispacecraft longitude (190°).

In this lit case, the match is not as good as the unlit case, and the data show a somewhat broader peak than that produced by the model. This is likely due to the inadequacy of the reflectivity and phase function of the planet model compounded by the low observer elevation angle. Note that the *Pioneer* reflectivity data for one belt and one zone were taken and averaged to give the reflectivity of the whole planet (Dones et al. 1993): that is, the model planet is uniformly reflective everywhere, north and south, with no banded structure. Also, the *Pioneer* data were modeled to derive a simple analytical form for the phase function, which was used in our ray-tracing experiments. Considering the lack of fidelity between the model and the real planet, the match in Figures 18 and 19 in both the lit and unlit cases is quite good. Determining the variation of reflectivity and phase function across the globe of Saturn is a cardinal goal of the Cassini imaging experiment (Porco et al. 2004). A more sophisticated planet model, based on Cassini results, will eventually be incorporated into future versions of the planetshine code.

Moving outward from the C ring to the B ring, Figure 20 shows a planetshine scan from Cassini images for the unlit (northern) side at 108,120 km. The data were modeled with two approaches. The results of a random box of particles are on the left, as above, but with particles ranging from 30 cm to 5 m in radius with a power-law index of $q = 2.8$. This is identical to that found for the B ring by French & Nicholson (2000) except that we have again truncated the upper limit from 20 m to 5 m. The vertical distribution of particles in the model uses an FWHM = 6 m. On the right, we show the results of ray-tracing boxes with "idealized wakes," with a vertical thickness of 20 m FWHM, a wavelength of 160 m, and a pitch angle of 15°, akin to what had been detected in the B ring by Colwell et al. (2007).

The morphology of the observed reflected planetshine peak is very similar to what is seen in Figure 18. The overall I/F is lower here for two reasons. First, the B ring is much more opaque than the C ring, so there is much less transmitted light (either direct sunlight or planetshine from the southern hemisphere). Second, the planetshine illumination on the rings falls off as roughly $1/r^3$ (a factor of $1/r^2$ due to the spreading of light with distance and a factor of $1/r$ due to the increasing angle of incidence on the ring plane), leading us to expect that this part of the B ring only gets about 60% of the planetshine illumination received by the C ring at 85,300 km.

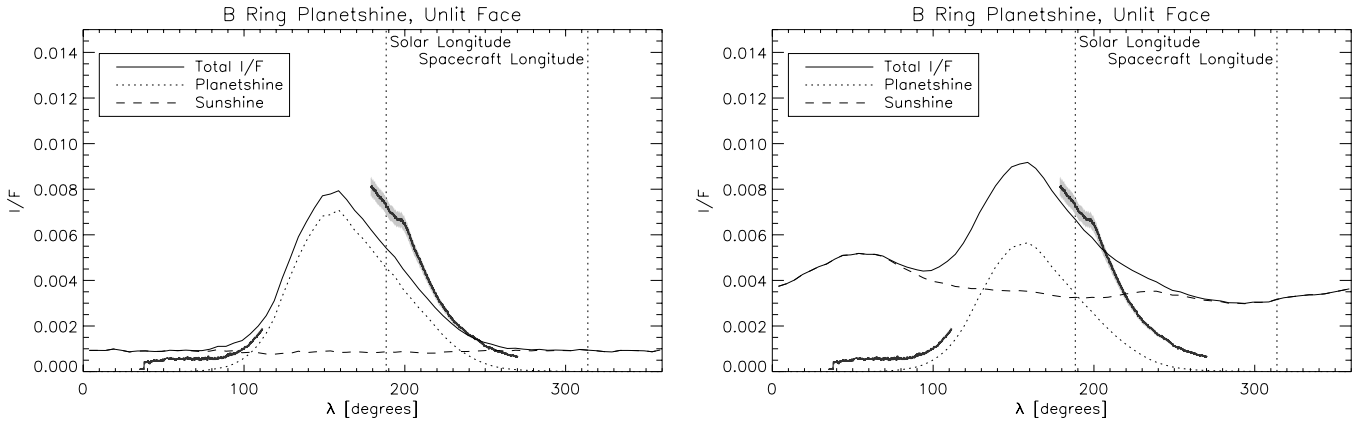

Figure 20. Data and model of planetshine for the unlit face of the B ring observed at a phase angle of 127°.6. Vertical lines have the same meaning as in Figure 18. The scan is taken at an orbital radius of 108,100 km. The albedo in both models is 0.6. The model in the left panel uses a spatially uniform distribution of particles (i.e., no wake-like structures are present), while the model on the right uses idealized wakes akin to those used by Colwell et al. (2007) and Hedman et al. (2007). Data are from Cassini images W1532506579 and W1532582920 (see Figure 18).

It is interesting that the planetshine data for the B ring, at least at longitudes far from the peak, are modeled best by the uniform boxes of particles and not by the wakes, and that the opposite is true near the peak. French et al. (2007a) found an azimuthal asymmetry in the inner B ring and a weaker asymmetry in the outer B ring, but little or no asymmetry in the central part of the B ring at low phase angles. At the higher phase angles observed in Cassini data, an unmistakable asymmetry is observed. It is likely that no wakes exist in this region of the B ring, as it is a region characterized by a great number of irregular structures with large variations in the optical depth, and that other types of azimuthal structures of different spatial scales are present and may cause part of the data/model discrepancy in this region of the rings. This topic will receive attention in future analyses.

4. DYNAMICAL RING SIMULATIONS

4.1. Basic Formulation

For many applications in the study of Saturn's rings, the use of random particle boxes in simulating the rings is inadequate. This is especially true when the rings are expected to have structures smaller than the scale of the box. To this end, we have customized the sophisticated *N*-body code `pkdgrav`, a numerical gravity solver first developed for cosmological modeling (Stadel 2001; Wadsley et al. 2004) in order to produce realistic particle distributions as inputs to the ray-tracing code. The code was adapted to treat hard-sphere collisions for planetesimal modeling (Richardson et al. 2000); a particle size distribution is easily accommodated. The main technical features of the code include a hierarchical tree algorithm for reducing the computational cost of interparticle force calculations and a complete parallel implementation for balancing work across an arbitrary number of processors. These features place `pkdgrav` among only a handful of truly parallel tree codes available for modeling complex systems of gravitationally and collisionally interacting particles.

We use the local "sliding patch" model for our simulations (Wisdom & Tremaine 1988; Richardson 1994; Salo 1995). In this model, the dynamics at a fixed orbital distance from the central body are represented by particles in a patch of arbitrary vertical dimension. The azimuthal and radial extent of the patch are small compared with the orbital distance but large compared with the radial mean free path of the particles inside it. The surrounding replica patches, with exactly the same particle distribution, are used to provide realistic boundary conditions. The assumption is that on this scale, the details of the structure inside a neighboring patch are unimportant; only the mean field matters (plus any physical contact when particles straddle the boundary so that momentum transport remains smooth). For consistency, the innermost and outermost replica patches must move relative to the central patches in accordance with the shear.

A supporting piece of software is used to generate initial conditions. This program takes as input a variety of desired ring parameters, including surface density, particle density, particle sizes, particle spins, patch dimensions, and starting velocity dispersions. Typically, our patch sizes are $4 \times 10\lambda_{\rm crit}$. Here, $\lambda_{\rm crit}$ is the value of the most unstable wavelength and is given by

$$\lambda_{\rm crit} = \frac{4\pi^2 G\Sigma}{\Omega^2}, \tag{29}$$

where Σ is the particle surface density and Ω is the angular speed of the patch. The large azimuthal dimension is needed to properly resolve the most unstable wavelength and to minimize the effect of particle "memory" following a boundary wrap. Particles are initially placed randomly in the patch, with an option for a dispersion in z provided by Gaussian deviates. Particle velocities are assigned using Gaussian deviates. The simulations are largely insensitive to the initial velocity dispersion and quickly (within 10 orbits) settle to equilibrium values. Particle spins start at zero, but particles can acquire spin during a collision through a user-assigned surface friction coefficient. The spins are continuously tracked and properly take into account the complications arising from the rotating frame of reference.

The equations of motion are given by the linearized Hill's formulation for the shearing sheet (Hill 1878; Wisdom & Tremaine 1988):

$$\ddot{x}_i = -\partial\Phi_i/\partial x + 3\Omega^2 x_i + 2\Omega\dot{y}_i, \tag{30}$$

$$\ddot{y}_i = -\partial\Phi_i/\partial y - 2\Omega\dot{x}_i, \tag{31}$$

$$\ddot{z}_i = -\partial\Phi_i/\partial z - \Omega^2 z_i, \tag{32}$$

where $\Phi_i = -\sum_{j\neq i} Gm_j/r_{ij}$ and r_{ij} is the separation between particles i and j. Φ_i is the gravitational potential on particle i due to all other ring particles, x is the radial direction, y is the orbital direction, and z is north. These equations are integrated in `pkdgrav` using a second-order leapfrog integrator (Richardson et al. 2000; T. Quinn et al. 2007, in preparation). We use a "kick-drift-kick" scheme: velocities are first kicked at a fixed

position for half a step, then positions are drifted for a full step at fixed velocity, and finally velocities are kicked the remaining half-step. The (constant) time step is chosen to be small compared to $2\pi/\Omega$ (the orbital period) or the dynamical time $1/\sqrt{(G\rho)}$ (ρ is the particle mass density), whichever is smaller, and is typically about 50 s. (The dynamical time is a rough measure of the interaction timescale of a self-gravitating system.) Gravity is calculated before each kick using a tree code that approximates the potentials due to distant groups of particles by multipole expansions about the group centers of mass, resulting in computation times that scale as order $N \log N$ but that give rise to small force errors (see Barnes & Hut 1986). The errors are controlled by a single parameter, the tree-opening angle, that determines how small and distant a group of particles must be to use the approximation (we use a value of 0.3 rad, a good compromise between speed and accuracy). Typical implementations expand the potentials to quadrupole order; `pkdgrav` expands to the hexadecapole order.

Collisions are predicted at the beginning of each drift step by keeping the particle velocities fixed and extrapolating the particle positions. Since this is a linear transformation, the time to surface contact between a pair of approaching particles is a simple quadratic expression. Potential colliders are found in order $N_s \log N$ time (N_s is the number of neighbors to check, typically ~32) using the tree. If the time to surface contact of a potentially colliding pair is found to be less than the size of the drift step, then a collision is performed. If more than one pair of particles satisfies this condition, the pair with the smallest collision time is processed first.

Once the collision outcome has been determined by applying user-selected restitution formulae, new collision circumstances are computed for the affected particles to ensure that all collisions are detected and treated in the correct order, even if particles are involved in more than one collision during the drift step.

Boundary conditions from the cosmology component of `pkdgrav` were modified for the sliding patch model to account for the shear. The boundary conditions in this case are time-dependent, making it necessary to compute the phase of the sliding patches when particles are near the boundary (either crossing the boundary or when searching for neighbors). Since replica patches have large opening angles as seen by most particles in the central patch, there is little additional cost for computing their contribution to the gravity field. For safety we typically use three rings of replicas, making 49 patches in all. Note that the Ewald correction used in `pkdgrav` (Hernquist et al. 1991; Stadel 2001) is not necessary in this case, since gravitational perturbations from the particles drop off rapidly with distance in the flattened disk geometry.

Runs are carried out 5–10 orbits beyond the time when the velocity dispersions achieve equilibrium, which is typically after ~5–10 orbits.

4.2. Ring Patch Simulations

In running ring patch simulations, among the first choices of input parameters are the particle physical characteristics, such as internal bulk density and size distribution. Our choices were guided by several important constraints. From the analysis of weak linear density waves in the mid-A ring observed in Cassini images (Tiscareno et al. 2007), the surface mass density of this ring region was found to be on average 430 kg m^{-2}. The small moons, Pan and Daphnis, orbiting within Saturn's outer ring region, have been found, within the uncertainties, to have densities comparable to their critical densities: that is, the density below which the ring material can no longer gravitationally accrete onto them (Porco et al. 2007). In the mid-A ring, critical densities are ~440–500 kg m^{-3}. The particle size distribution for this ring region was determined to be a differential power law with an index $q = 2.75$, a lower limiting radius of 30 cm, and an upper limit of 20 m (French & Nicholson 2000). However, as noted earlier, there is significant uncertainty regarding the upper-limiting particle size since the presence of wake structures themselves, with thicknesses of ~20 m, likely contaminates the determination of this quantity and on physical grounds, an upper limit of ~5 m may be more plausible as this is the expected natural scale of self-gravitational disturbances in Saturn's A ring (Shu 1984).

We have found, in fact, that all these constraints can be consistently accommodated if we make the upper-limiting particle radius 3 m. Anything larger either violates the surface mass density constraint for an internal density of 420 kg m^{-3} (i.e., a 5 m upper limit forces this quantity to be closer to 610 kg m^{-2}) or violates the internal density if we constrain the surface mass density to be 430 kg m^{-2} (i.e., the internal density decreases to 280 kg m^{-3}, which is unacceptably lower than the critical density). For the geometries we consider in this paper, light scattered from a particle size distribution with a 5 m upper limit, an internal density of 420 kg m^{-3}, and a surface mass density of 610 kg m^{-2} is photometrically indistinguishable from that scattered from one with a 3 m upper limit, an internal density of 420 kg m^{-3}, and a surface mass density of 430 kg m^{-2} (see Section 6). Nonetheless, we have chosen the latter set of parameters for our simulations as those are consistent with all known constraints.

Figure 21 shows "snapshots" taken from several dynamical simulations of a patch of Saturn's A ring at a mean orbital distance $a = 128{,}000$ km and with mean motion $\Omega = (GM_{\rm Saturn}/a^3)^{1/2} = 1.345 \times 10^{-4}$ rad s^{-1} using approximately 60,000 particles of density 420 kg m^{-3} ranging in size from 0.3 to 3 m as selected uniformly from a power-law distribution with $n(r)\,dr \propto r^{-q}dr$, where $q \sim 2.75$. The ring patch code can, in principle, follow millions of particles (Perrine & Richardson 2006) in reasonable compute times, but only 60,000 were required to simulate the A ring using realistic parameters. All simulations were carried out for at least 15 orbital periods, comfortably beyond the point where the velocity dispersions reached equilibrium (about 5–10 orbits); some of the snapshots were taken from time steps as early as 12 orbits into the simulation. The patch dimensions in both cases were $4\lambda_{\rm crit} \times 10\lambda_{\rm crit}$, where $\lambda_{\rm crit} = 4\pi^2 G\Sigma/\Omega^2 = 62.6$ m is the critical Toomre wavelength for our chosen value of surface mass density $\Sigma = 430$ kg m^{-2}. That is, the patch dimensions were $\Delta_y = 626$ m by $\Delta_x = 250$ m. Particles were initially distributed uniformly in the plane of this patch, with a random uniform vertical component of $\pm$ 5 m. The corresponding dynamical optical depth $\tau = 0.6$ and volume filling factor = 0.088. Initial velocities were chosen uniformly between 0 and $\Omega\bar{R}$ in the radial direction and between 0 and $\Omega\bar{R}$ in the azimuthal and vertical directions, where $\bar{R} = 0.59$ m is the mean particle radius. These initial dispersions were chosen deliberately to be far from the equilibrium values, which turned out to be about a factor of 10 larger than the starting values. For each run, we used a time step of 46.3 s (0.001 of an orbital period and 0.01 of the dynamical time for particles of our chosen mass density).

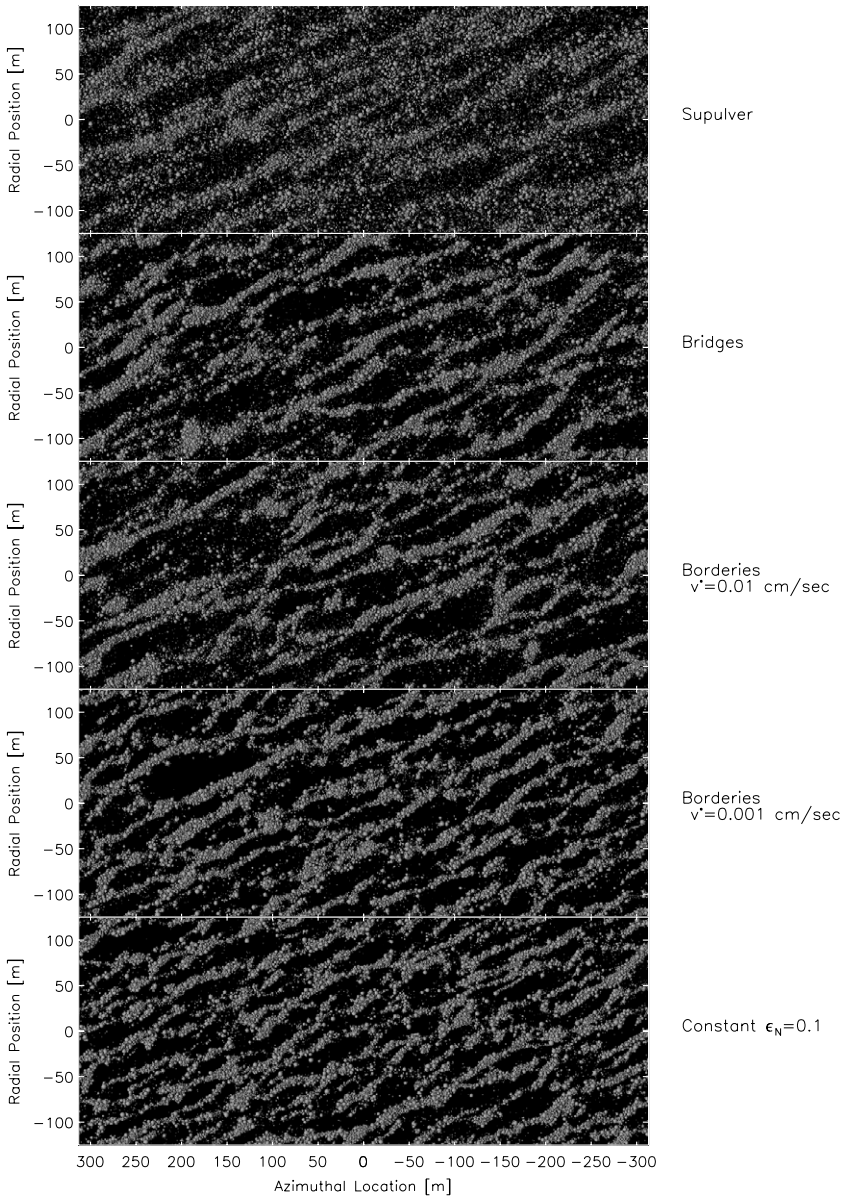

Figure 21. Five large-scale dynamical "ring-patch" simulations showing particles in Saturn's mid-A ring at 128,000 km after at least 12 complete orbits. The simulation cell is $\Delta_y = 626$ m by $\Delta_x = 250$ m. The radial direction is up; the orbital motion is to the left. At this equilibrated stage, the evolution of the system is characterized by the rapid (∼1 orbit) formation, dissolution, and reformation of filamentary wake-like structures with a pitch angle of ∼25° to the azimuth and an average separation of ∼65 m. This is roughly the critical wavelength (Julian & Toomre 1966), in agreement with theory. For all these simulations, ring particle and disk parameters were taken to be those expected for the middle of the A ring: a particle size distribution of a power-law index, $q \sim 2.75$, with $r_{\rm min} = 0.3$ m and $r_{\rm max} = 3$ m, a surface mass density ∼430 kg m^{-2}, particle internal density ∼420 kg m^{-3}, and a dynamical optical depth $\tau_d \sim 0.6$. Different elasticity laws were used for these simulations. From top to bottom, the elasticity laws were velocity-dependent coefficient of restitution laws found by Supulver et al. (1995) (uppermost) and Bridges et al. (1984) (second from top) in laboratory experiments on smooth ice particles; velocity-dependent laws of the form used by Borderies et al. (1984) for smooth ice spheres with v* = 0.01 cm s^{-1} and v* = 0.001 cm s^{-1} for the middle and second-from-the-bottom ring patches; and a constant restitution law with $\epsilon_n = 0.1$ was used for the bottom ring patch. All simulations had $\epsilon_t = 0.9$.

However, the differences among the simulations lie in the law used to describe the elasticity of the particles as a function of their collision speeds. In the upper simulations of Figure 21, we adopted two coefficient of restitution laws commonly in use: that due to Supulver et al. (1995) and the other due to Bridges et al. (1984). Both of these have the form

$$\epsilon_n(v_n) = \left(\frac{v_n}{v_c}\right)^b, \tag{33}$$

where ϵ_n is the normal coefficient of restitution, v_n is the magnitude of the normal component of the radial velocity expressed in cm s^{-1}, and $v_c = 0.0077$ cm s^{-1} and $b = -0.234$ for Bridges and $v_c = 0.01$ cm s^{-1} and $b = -0.14$ for Supulver.

Both laws, displayed in Figure 22, were determined in laboratory collision experiments on smooth ice spheres, but in one case (Bridges) the particles were frosty with temperatures ∼ 200 K, and in another (Supulver) frost-free with temperatures ∼ 100 K.

For the second set of simulations, we adopted a restitution law for the particles that yields a smaller ϵ_n for the higher velocity particles in order to explore the effects of higher inelasticity in clearing out the small interwake particles. Here, we assumed the functional form derived by Borderies et al. (1984) for smooth

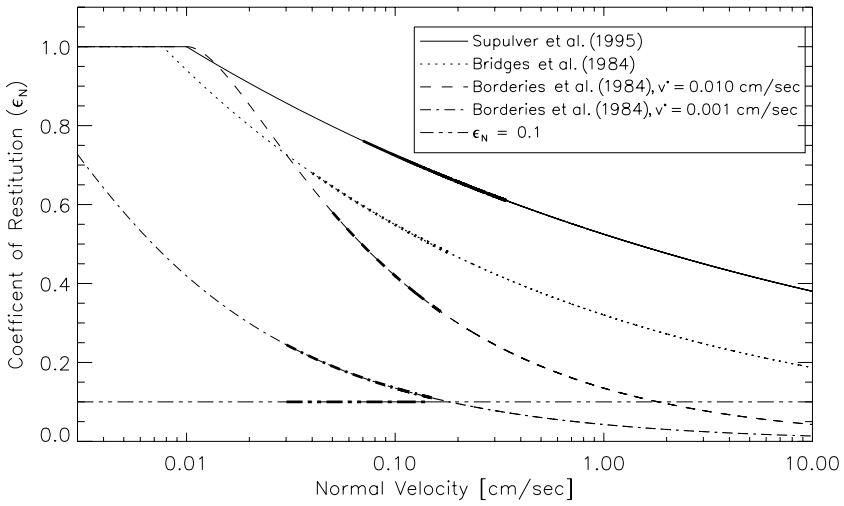

Figure 22. Restitution laws mentioned in this work. The bulk of the smallest particles in each of the simulations performed using these laws falls within the velocity range indicated by the bold sections on each curve.

ice spheres from

$$\epsilon = \left\{ -\frac{2}{3}\left(\frac{v^*}{v}\right)^2 + \left[\frac{10}{3}\left(\frac{v^*}{v}\right)^2 - \frac{5}{9}\left(\frac{v^*}{v}\right)^4\right]^{1/2}\right\}^{1/2}. \quad (34)$$

However, to explore greater inelasticity, we have altered the point at which the particles transition from purely elastic to inelastic behavior from the Borderies et al. (1984) value of $v^* = 0.03$ cm s^{-1} to $v^* = 0.01$ cm s^{-1} in one case, in line with the transition speed found by Supulver et al. (1995), and to $v^* = 0.001$ cm s^{-1} in another case to test even smaller elasticities. These smaller transition speeds, which produce lossier particles in the range of speeds relevant for the mid-A ring, may not be unreasonable. The particle surfaces are very likely to be rough, which serves to lower the coefficient of restitution (Borderies et al. 1984), as does the presence of a regolith (Colwell & Taylor 1999; Colwell 2003). Additionally, the particles are very porous: an internal mass density of 420 kg m^{-3} yields a particle with ∼43% void space. Collisions between such particles may be characterized by compression of the surface material at the contact point into void space followed by very little rebound.

For completion, we also tried a constant coefficient of restitution, $\epsilon_n = 0.1$.

For all these restitution laws, which are shown in Figure 22, we adopted a tangential coefficient of restitution, $\epsilon_t = 0.9$, as measured by Supulver et al. (1995). (Note that no other laboratory experiment obtained a measure of ϵ_t.)

Gravitational wake structures are clearly seen in all the ring patch simulations utilizing these restitution laws, as shown in Figure 21, after at least 12 orbital periods and long after the system has equilibrated. What is visually very noticeable is that for the lossier restitution laws, the interwake particles are less abundant than in the Supulver case. We find that in the Supulver case, it is the smallest fastest particles that lie in between the wakes and when we assume greater inelasticity, their velocity dispersions are also reduced (Figure 23): the peaks in the velocity distributions for the particles in the size range from 0.3 to 0.5 m—that is, the smallest particles—are shifted from ∼0.18 cm s^{-1} for the Supulver law down to a peak relative velocity of ∼0.1 cm s^{-1} for both the Bridges and $v^* = 0.01$ cm s^{-1} laws, and a bit farther to 0.08 cm s^{-1} for the lossier $v^* = 0.001$ cm s^{-1} and $\epsilon_n = 0.1$ laws. In Figure 22, we have indicated the FWHM limits of the small particle velocity distributions, where most of the small particles fall in relative velocity, on the appropriate restitution law. The fact that the large jump in energy loss (Figure 22) between the $v^* = 0.01$ cm s^{-1} and $v^* = 0.001$ cm s^{-1} simulations does not result in a large jump in peak velocity dispersion is a result of the fact that both velocity shear across the rings and ring particle self-gravity will keep the ring particles stirred above a minimum velocity. In the case of the small particles in our simulations, this minimum is predominantly set by the escape speed of ∼0.03 cm s^{-1}.

For all of these laws, the velocity dispersions of the largest particles, which are found within the wakes, remain approximately the same, with an average of ∼0.11 cm s^{-1}.

There are even slight but noticeable differences in the four lossier simulations. Bridges and $v^* = 0.01$ look similar to each other in the number of remaining interwake particles, and $v^* = 0.001$ and $\epsilon_n = 0.1$ also look similar to each other in this regard, though the latter set looks clearer of interwake particles than the former, and there are differences in scale of the wake structures, and the sizes of the voids in between them, in comparison with the members of the latter set. Moreover, these gross differences between the different simulations are maintained when one examines frames taken at different time steps than those shown in Figure 21, as long as the frames come from times past equilibration.

These are all critical factors in the analysis and modeling of the A ring azimuthal brightness asymmetry presented in Section 5.

5. LOW-PHASE LIGHT SCATTERING: THE AZIMUTHAL ASYMMETRY

To begin our investigation of the A ring azimuthal brightness asymmetry, a photometric phenomenon that is one of the manifestations of self-gravity wakes in the rings (e.g., Dones & Porco 1989), we examine two different lit-face low phase geometries: a Voyager geometry, at low sun and observer (or spacecraft) elevation angles (∼10°), and a Cassini geometry, at higher Sun and spacecraft elevation angles near 22°. In the upper part of Figure 24, we present a scan of brightness at low phase around the A ring as measured in Voyager images FDS 43650.10

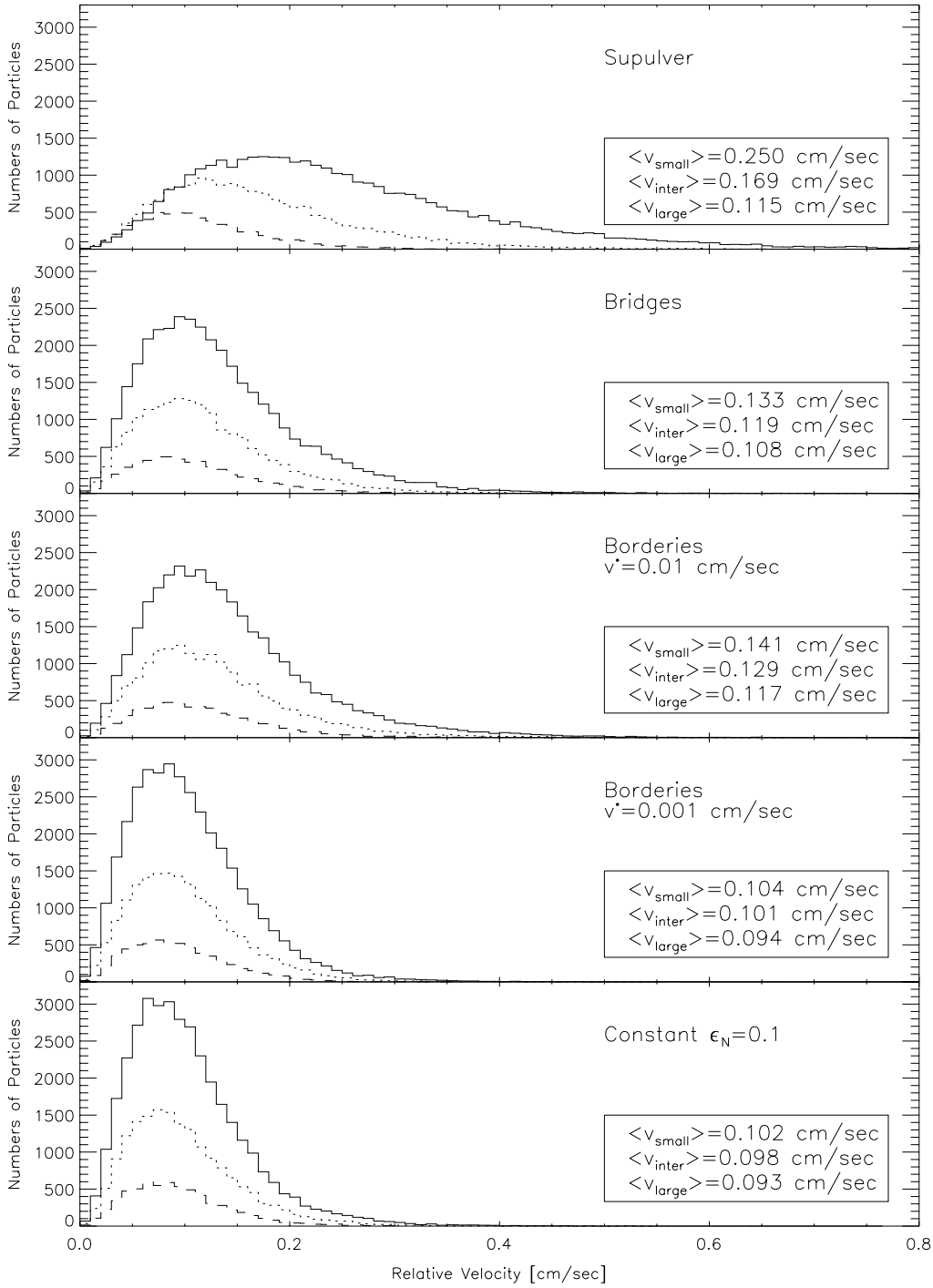

Figure 23. Relative velocities for small- (< 50 cm), large- (> 1 m), and intermediate-sized particles in the five simulations shown in Figure 21.

and FDS 43650.22 (one of the left ansa and one of the right ansa) at a semimajor axis of 128,900 km. Error bars on the data curves show the uncertainties (∼10%) inherent in the calibration of Voyager images. In the lower panel, we present a scan around the A ring at a semimajor axis of 128,000 km, taken from 19 separate Cassini clear-filter images on 2005 June 7 while the spacecraft was at a distance of 986,000 km (∼16 Saturn radii). The calibration uncertainty of the Cassini clear filter is ∼5%. In both scans, longitudes lacking data belong to parts of the ring that are obscured by Saturn, in the planet's shadow or in front of the planet, where the planet's disk interferes with the measurements.

In comparing these scans, there are two obvious differences between Cassini and the Voyager (and Earth-based) observations of the asymmetry: the location of the brightness extrema and the variation between the right (<180°) and left (>180°) sides of the ring.

The first minimum in the Cassini data appears at about 77°, compared to 67°. This 10° shift is the signature of the increasing separation in longitude of the Sun and spacecraft. There is a minimum in the brightness where the observer looks along the long axis of the wakes, because gaps in this viewing geometry take up a larger fraction of the projected area as seen by the observer. Moreover, the gaps, having less material, scatter

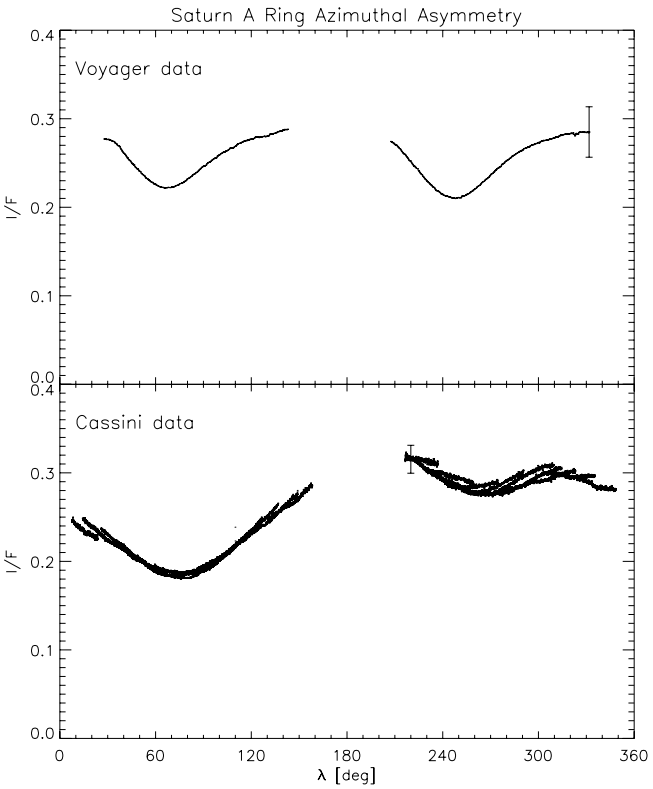

Figure 24. Top: the azimuthal brightness asymmetry in the A Ring at an orbital distance of 128,900 km, as observed in Voyager clear-filter images FDS 43650.10 and FDS 43650.22. The difference in Sun and spacecraft longitudes was 8.°2, the subspacecraft latitude was 10.°8 (so that the observer elevation angle on the ring ranges from 10.°7 to 11.°0), and the subsolar latitude was 7.°9. The phase angle was 8.°05. The error bar on the data shows the estimated absolute uncertainty in the Voyager clear-filter calibration of ∼10%. Bottom: the A ring azimuthal brightness asymmetry seen from Cassini at an orbital distance of 128,000 km in clear-filter images taken on 2005 June 7. The difference in Sun and spacecraft longitudes is 23.°2, the subspacecraft and subsolar latitudes are both −21.°5, and the observer elevation angle on the rings varies from −19.°0 and −24.°6. The phase angle is 21.°5. The error bar on the data show the absolute uncertainty in the calibration of the Cassini clear filter of ∼5%.

less light to the observer, so the brightness is consequently reduced. The same thing happens when the sunlight falls on the rings in the same orientation: more of the sunlight passes straight through the gaps, leaving less to scatter to the observer, regardless of where the observer is. In principle, we expect there to be two minima at around 77°: one for the observer (which should occur between 65° and 70°) and one for the Sun which has a 23° offset from the observer's minimum, and should be ∼90°. In reality, the wakes have a distribution of orientations that spreads both minima and blurs them into one minimum at approximately their average longitude.

There is also a marked difference in brightness between the two sides of the ring. A possible explanation for the left/right amplitude difference may rest with differences in the emission angle. The spacecraft's proximity to the ring can lead to the emission angle from the rings varying significantly with longitude around the ring. However, the two minima are located near ±90° so that these locations on the ring are nearly equidistant from Cassini at the time of observation. The slight difference in distance causes a change in the emission angle of only 69.°6–70.°4. As Figure 10 shows, this is insufficient to cause the ∼50% differences in amplitude seen in the scan. The wake structures may complicate this: small differences in the emission angle may cause larger variations in I/F than implied by the homogeneous models. This will receive further attention in future work.

To determine the particles' elastic and photometric characteristics that fit these data the best, we ray-traced the five different dynamical simulations of the mid-A ring (orbital distance of 128,000 km) shown in Figure 21, assuming the illumination and viewing geometries appropriate for the two (Voyager and Cassini) observations. In all ray-tracing runs, we used a dense grid of source photons with a spacing of 1 m, 96 child photons, and a scattering order of 3. We also assumed in every case the phase function found for the middle of the A ring by Dones et al. (1993): that is, a Callisto-like power-law phase function with an index $n = 3.092$.

Note that the Voyager data scan was taken at 128,900 km; the Cassini scan was taken, and all the ring patch simulations were done, at 128,000 km. At the former orbital distance from Saturn, the amplitude of the asymmetry (defined to be 2(peak − trough)/(peak + trough) is ∼3% larger than it is at 128,000 km (Dones et al. 1993). Consequently, we corrected the amplitude of our Voyager scan to a distance of 128,000 km by decreasing its amplitude by 3%; the Voyager scan adjusted in this way was used in the fitting of the ray-tracing models to the data.

It became obvious upon initial comparison of data and models that there is a small discrepancy of ∼5° in the azimuth of the troughs between the models and the data scans for both Voyager and Cassini geometries. This offset was found by others examining the asymmetry in *HST* (and therefore low phase) images (French et al. 2007a). The angular phase of the minimum in the model curve is dependent on the cant of the wakes in the simulations. The sign of the angular mismatch implies that the wakes in our simulation are not orbitally sheared as much as (or are more radial than) the real wakes. The ring patch code does not include the nonspherical gravity harmonics in the planet's gravitational field, but a simple calculation of the effects on the orbital shear in the mid-A ring of adding J_2 and J_4 yields a change significantly less than 1°. Also, while the size of the ring patch can affect the tilt of the simulated wakes in the case where the patch is not sufficiently large, our boxes are large enough to avoid this problem. We do not yet know the exact cause of this small mismatch but we note (below) that it changes slightly (ranging from 5° to 8°) for different simulations and fits. We intend to investigate this offset in future studies in which we will explore the effects of varying the tangential coefficient of restitution, ϵ_t, and examine the effects of more complicated particle structures (Richardson 2008). Nonetheless, we believe that the discrepancy is small enough not to undermine the arguments presented here.

The final values determined for the particle albedo and angular shifts from the fits to the Voyager and Cassini data of all the models examined here were those that yielded minimum residuals between the data and model, normalized by the errors in the data: that is, 10% for Voyager (Dones et al. 1993) and 5% for Cassini. These best-fitting models and data are shown in Figures 25 and 26.

Clearly, in the Voyager geometry, the model using the Supulver restitution law does not give adequate results: there is a large mismatch between the model amplitude and the observations. We also ran models with a size-distribution power-law index of $q = 3$, but found an insignificant change in the model amplitude. This discrepancy has been known for some time, and it has been long surmised that its cause was related to an excessive abundance of small particles in between

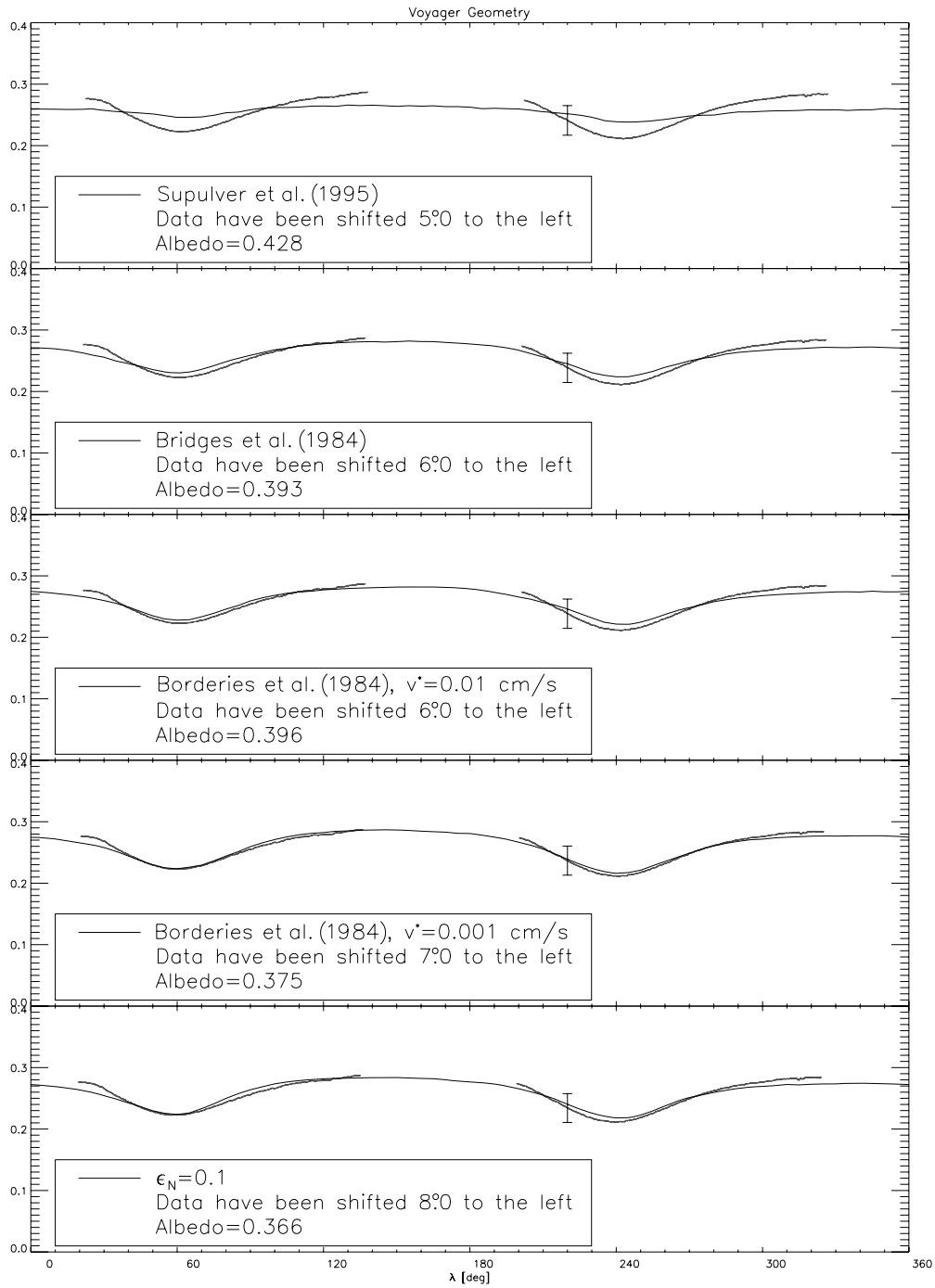

Figure 25. The best-fit models produced by ray tracing the five simulated ring patches shown in Figure 21 using the geometry appropriate for the Voyager data, together with the observed Voyager light curve adjusted in amplitude (as described in the text) for an orbital position of 128,000 km. The best-fit albedo and angular shift are given in the legend to each figure.

the simulated wakes, which has the effect of reducing the wake/interwake contrast and smoothing out the light curve (Porco et al. 2003). It was for this reason that restitution laws that yielded greater inelasticity at velocities appropriate to these interwake particles, and one that cleared out the small interwake particles, were used in running additional dynamical simulations. The normalized residuals for the Supulver model fit to the Voyager data are RMS = 0.56.

The matches in amplitude using the more lossy restitution laws are better than for Supulver but some are better than others. In the Voyager case, the best-fitting model in terms of shape, amplitude, and minimum residuals is the $v^* = 0.001$ cm s^{-1} law. With a best-fitting albedo $A = 0.38 \pm 0.04$ and an angular shift of $\sim 7^\circ$, it produces the lowest normalized residuals of RMS = 0.14. The formal albedo uncertainties are 1σ and determined by the shift in the fitted albedo that produces an increase of 1 in the normalized residuals (Bevington 1969).

Each of the panels in Figure 21 is a single time step near 12 orbits in a dynamical simulation that ran for at least 15 orbits, far past equilibration of the system. The wake structures in these simulations are transient and form and shear on timescales of an orbit, but the overall character of the ring patch to the eye

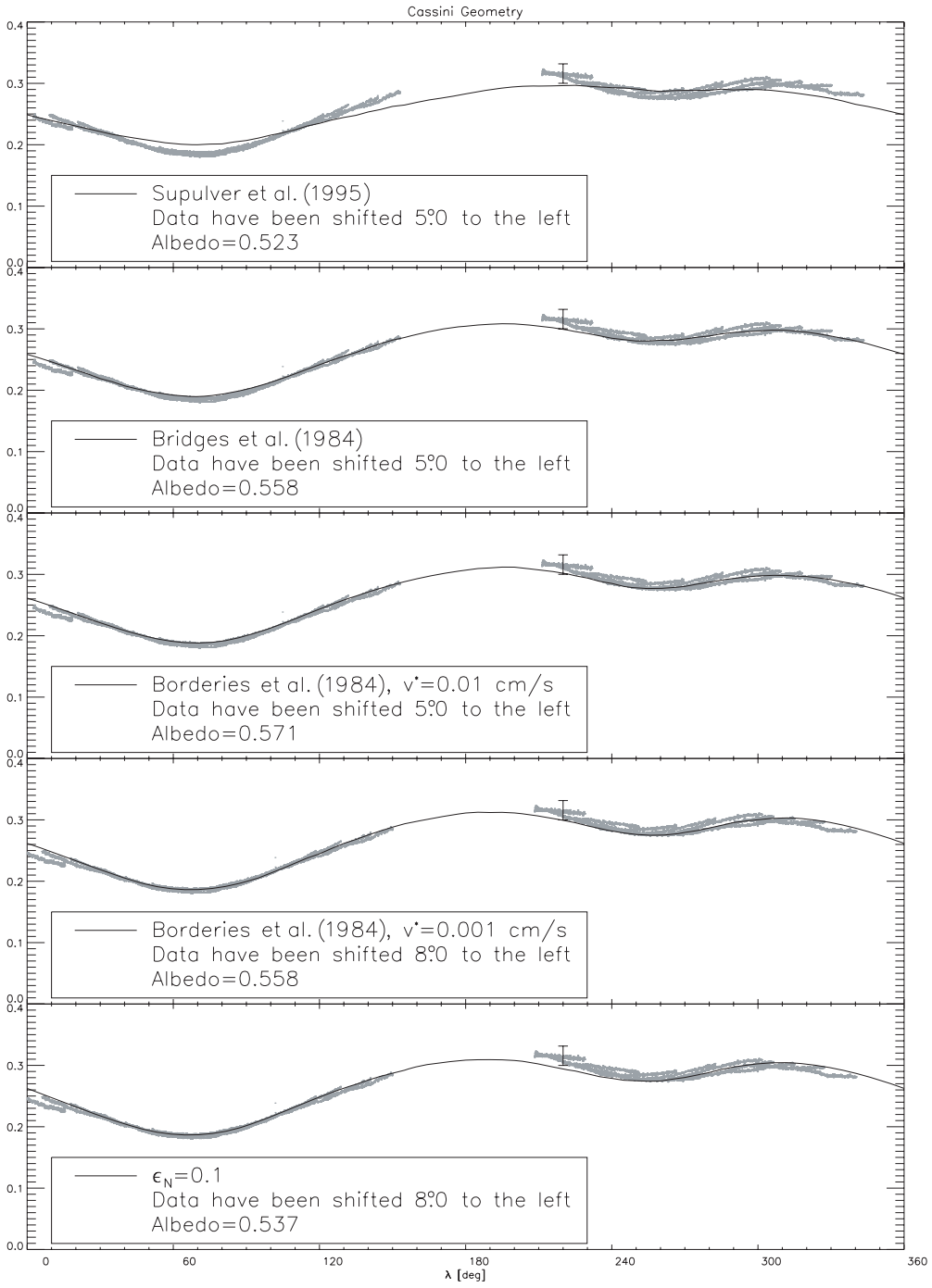

Figure 26. The best-fit models produced by ray tracing the five simulated ring patches shown in Figure 21 using the geometry appropriate for the Cassini data, together with the observed Cassini light curve. The best-fit albedo and angular shift are given in the legend to each figure.

is largely the same. Nonetheless, to determine the variation in our ray-tracing results due to the transient nature of the "scenes" in Figure 21, we chose a different time step in the $v^* = 0.001$ cm s^{-1} simulations than that shown in Figure 21 and ray-traced it at the Voyager and Cassini geometries. The resulting curves are displayed next to the nominal curves in Figure 27 and illustrate the level of variation one can expect in the model light curve for any given restitution law model over the course of a simulation. In fits of the Voyager and Cassini data to their respective ray-traced curves extracted from the two different time steps represented in Figure 27, the minimum normalized residuals varied ~20% for both Voyager and Cassini geometries. When six different postequilibration time steps from the same simulation ($v^* = 0.001$ cm s^{-1}) were chosen for ray tracing and intercomparison, the standard deviation of the residuals from the mean was $\sigma \sim 14\%$. Thus, a variation of ~20% in the minimum normalized residuals obtained from different restitution models fitted to the same data set, which is $\sim 1.5\sigma$ from the mean residuals, and the concomitant differences in the shapes of the resulting light curves as shown in Figure 27 are not statistically significant.

The remaining velocity-dependent restitution models have increased normalized minimum residuals over those of the $v^* = 0.001$ cm s^{-1} model by a factor significantly greater than

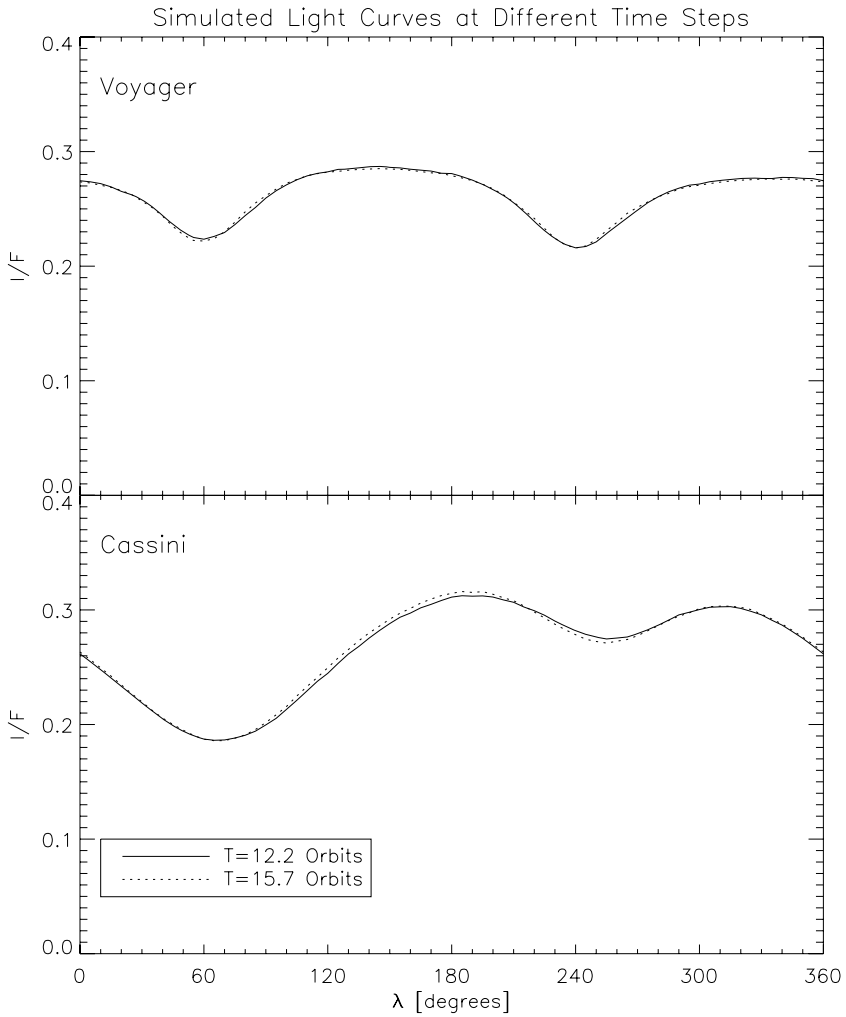

Figure 27. Ray-tracing results for both the Voyager and Cassini geometries, comparing model light curves at two different time steps—12.2 and 15.7 orbits—in the $v^* = 0.001$ cm s^{-1} simulation. One of these time steps ($T = 12.2$ orbits) is the second-from-the-bottom ring patch shown in Figure 21.

20%—that is, ∼60% for $v^* = 0.01$ cm s^{-1} and ∼80% for Bridges—but not different from each other by more than 20%. The constant $\epsilon_n = 0.1$ model had minimum residuals ∼50% greater than the $v^* = 0.001$ cm s^{-1} model.

Thus, we conclude that, of all the models we tried, the best-fitting model for the ring region at 128,000 km observed in the Voyager geometry is the $v^* = 0.001$ cm s^{-1} restitution law and yields an angular shift of ∼7° and an $A = 0.38 \pm 0.04$. This is only somewhat lower than the albedo observed for the mid-A ring through the Voyager clear filter (with $\lambda_{\rm eff} = 0.49\ \mu$m), $A = 0.49$ (Figure 14 of Dones et al. 1993), when 2σ uncertainties are considered.

In the Cassini case, we can also confidently reject the Supulver model; it cannot reproduce the shape or amplitude of the Cassini light curve and its residuals are relatively large: RMS = 0.70. The more lossy velocity-dependent models do much better but which of these is best is less clear: the variation in normalized minimum residuals is no larger than 13% among them, and their average is $\overline{\rm RMS} = 0.39$. The constant $\epsilon_n = 0.1$ law yields residuals even larger: RMS = 0.48. So, at present, the data extracted from Cassini images cannot distinguish among any of the remaining laws—the constant ϵ_n, Bridges, $v^* = 0.01$ cm s^{-1}, and $v^* = 0.001$ cm s^{-1} laws —though the velocity dependent ones seem marginally better. The best-fit albedos for these velocity-dependent models are $A \sim 0.56 \pm 0.04$, consistent with the albedo, $A = 0.58$, derived in the red region of the spectrum sampled by the Cassini clear filter for this region of the rings (Porco et al. 2005).

6. SUMMARY AND DISCUSSION

We have developed two computer codes that form the basis of a technique for probing the physical structure and particle properties in planetary rings from their light-scattering behavior. Our ring-patch code realistically simulates a patch of colliding and self-gravitating particles in orbit around a planet and readily produces the transient, 100–200 m shearing agglomerations of particles called "self-gravity wakes" in Saturn's rings that we have demonstrated here are responsible for the azimuthal brightness asymmetry observed over the past 50 years in Saturn's A ring, and clearly seen in Voyager, *HST*, and Cassini images of the ring.

We have also developed a deterministic ray-tracing code that "shoots" light rays into a box of particles having predetermined photometric properties and distributed throughout the box either arbitrarily—for example, randomly or in the form of idealized wake structures—or realistically by our ring-patch code. It can simulate light scattering over a wide range of geometries, and successfully accounts for direct sunshine and sunlight reflected off the planet and onto the rings.

Our technique has been validated in comparisons of our results with those of other, accepted analytic or seminumerical techniques, such as classical single-scattering calculations and numerical adding/doubling methods.

We can reproduce the absolute reflectivity, I/F, of a region in Saturn's outer A ring, beyond the Encke gap, observed in Cassini low- and high-phase images using exceedingly thin rings ($\sim$10 m vertical thickness), a particle albedo of $A = 0.63 \pm 0.03$, and an empirical, power-law phase function with an index $n = 2.624\ldots$, more forward-scattering than we find for the mid-A ring. We also reproduce the brightness observed in Saturn's low optical depth C ring at low, intermediate, and high phases using an albedo of $A = 0.32 \pm 0.02$ and a Callisto-like phase function with index $n = 3.092$. Because of its low optical thickness, we cannot discern via this technique the vertical thickness of the C ring: thin or thick models might apply. We can also reproduce a suite of photometric observations not explained by the predictions of standard radiative transfer applied to classical rings.

Our findings here now allow ring thickness to be used as a parameter to explain certain Voyager photometric observations of Saturn's A ring, as has been suggested by others (Dones et al. 1993; Porco et al. 2001). Saturn's rings may in fact be darker at high phase than predicted by classical models because they are very thin. Observations of brightness variations across the B ring, which have been interpreted in terms of variations in particle albedo across the ring (Estrada & Cuzzi 1996), may well also have a component attributable to ring thickness instead. We will investigate this suggestion in the future.

We have made considerable progress in determining the elastic and photometric properties of particles in the mid-A ring from modeling of the well-known azimuthal brightness asymmetry observed there. We find that to reproduce the shape and the amplitude of the A ring light curve in both Voyager and Cassini low-phase, lit-face geometries requires a velocity-dependent coefficient of restitution that yields considerably more energy loss at the velocity dispersions appropriate for the small particles in the rings than is produced by the most recent laboratory measurements on ice (Supulver et al. 1995) and closer to but still more lossy than is produced by the original laboratory measurements (Bridges et al. 1984). Though useful in rejecting the Supulver model, the Cassini measurements used in this study were unfortunately not able to discriminate among the lossier restitution laws—that published by Bridges et al. (1984), or those given by the Borderies et al. (1984) law with $v^* = 0.01$ cm s^{-1} or $v^* = 0.001$ cm s^{-1}, or a law assuming a constant $\epsilon_n = 0.1$. We suspect that in future work, by using the numerous Cassini images now available over a range of illumination and viewing geometries, and utilizing improved photometric calibration, this circumstance will considerably improve.

For the moment, it is the Voyager data in the mid-A ring that provide the greatest leverage in determining the particle elastic properties and these data single out the $v^* = 0.001$ cm s^{-1} law as preferred over the others. This law yields a decrease in the coefficient of restitution for normal collisions, ϵ_n, at the velocity dispersions in question (Figure 22) as large as a factor of $\sim$5 below those determined from the Supulver model (compare $\epsilon_n = 0.15$ for the former to $\epsilon_n = 0.75$ for the latter at $\sim$0.1 cm s^{-1}) and a factor of $\sim$3.5 below the Bridges model (compare $\epsilon_n = 0.15$ for the former to $\epsilon_n = 0.55$ for the latter at the same speed). The Cassini data are at least consistent with these results.

The exact shape of the elasticity law beyond the range of velocity dispersions applicable to Saturn's rings is of course not addressed by this work. Other laws that behave very differently outside the relevant velocity range, and yet yield equivalently low and velocity-dependent coefficients of restitution within the relevant velocity range as that produced by the Borderies $v^* = 0.001$ cm s^{-1} law used here, may work just as well. Regardless of the exact shape of the elasticity law, our findings point to ring particles whose elastic properties are likely to be velocity-dependent and whose energy loss in mutual collisions, $\left(1 - \epsilon_n{}^2\right)$, is $\sim$40% greater than previously found in models of the A ring azimuthal brightness asymmetry (French et al. 2007b).

It is important to note that all the laboratory experiments were performed on relatively smooth spheres of solid ice. The Bridges experiments were performed on frosty warm (200 K) icy spheres; the Supulver experiments were done on colder (100 K) frost-free spheres. However, real particles in Saturn's rings, which are closer to 100 K and may be frosty, also undoubtedly have nonideal, rough surfaces for which collisions at contact points having a radius of curvature smaller than that of the particle will yield greater loss than collisions on smooth spheres (Borderies et al. 1984). Moreover, collisions between particles having a regolith (Colwell & Taylor 1999; Colwell 2003) or large porosity (and therefore a great percentage of void space) will also produce greater inelasticity, as some fraction of the energy of collision will be used to compact the material with very little rebound. Together, these processes may make for extremely inelastic particles.

In the future, we will extend our work on Cassini images of Saturn's rings to a variety of resolutions, geometries, and ring regions, as well as improve the image calibration in order to reduce measurement uncertainties in these data. We will also investigate the trade-off between increased inelasticity and particle size distribution in refining our model for the A ring asymmetry and, in turn, the estimates of energy loss as a function of velocity dispersion. And we will investigate the source of the angular offset between the observations and our models and its effects on the model results. Nonetheless, our results that the particles in Saturn's rings are more lossy than previously found should prove significant in the evaluation of the transfer of angular momentum and energy across Saturn's rings, both in perturbed and nonperturbed regions, and ultimately in studies of ring age, evolution, and lifetime.

The research presented in this paper was primarily supported by NASA grants PGG NAG5-4451 and CDAP NNXO8AP84G; support also came from the Cassini project. D. Richardson and T. Quinn acknowledge support from National Science Foundation Knowledge and Distributed Intelligence and Planetary Formation programs and from the NASA Applied Information Systems Research program. M. Pantazopoulou is acknowledged for her initial ground-breaking work in the formulation and development of the ray-tracing code. T. J. J. Kehoe is acknowledged for debugging an earlier version of the ray-tracing code. We acknowledge J. Colwell, for providing information derived from Cassini UVIS data prior to publication and also for an excellent thorough review, and J. Spitale, for developing the image analysis tool, MINAS, used in this work.

REFERENCES

Barkstrom, B. R. 1973, J. Geophys. Res., 78, 6370
Barnes, J., & Hut, P. 1986, Nature, 324, 446

Bevington, P. R. 1969, Data Reduction and Error Analysis for the Physical Sciences (New York: McGraw-Hill)
Borderies, N., Goldreich, P., & Tremaine, S. 1984, in Planetary Rings, Unsolved Problems in Planetary Ring Dynamics (Arizona: Univ. of Arizon Press), 713
Brahic, A. 1977, A&A, 54, 895
Bridges, F., Hatzes, A., & Lin, D. 1984, Nature, 309, 333
Chandrasekhar, S. 1950, Radiative Transfer (Oxford: Clarendon)
Colombo, G., Goldreich, P., & Harris, A. 1976, Nature, 264, 344
Colwell, J. E. 2003, Icarus, 164, 188
Colwell, J. E., Esposito, L. W., & Sremcevic, M. 2006, Geophys. Res. Lett., 33, L07201
Colwell, J. E., Esposito, L. W., Sremcevic, M., Stewart, G. R., & McClintock, W. E. 2007, Icarus, 190, 127
Colwell, J. E., & Taylor, M. 1999, Icarus, 138, 241
Cooke, M. 1991, PhD thesis, Cornell University
Cuzzi, J. N. 1985, Icarus, 63, 312
Daisaka, H., Tanaka, H., & Ida, S. 2001, Icarus, 154, 296
Danielson, G., Kupferman, P., Johnson, T., & Soderblom, L. 1981, J. Geophys. Res., 86, 8683
Déau, E., Charnoz, S., Dones, L., Brahic, A., & Porco, C. 2006, BAAS, 38, 577
Déau, E., Charnoz, S., Dones, L., Brahic, A., & Porco, C. C. 2008, Icarus, submitted
Dones, L., Cuzzi, J., & Showalter, M. 1993, Icarus, 105, 184
Dones, L., & Porco, C. 1989, BAAS, 21, 929
Doyle, L. R., Dones, L., & Cuzzi, J. N. 1989, Icarus, 80, 104
Estrada, P., & Cuzzi, J. 1996, Icarus, 122, 251
Franklin, F., & Cook, F. 1965, AJ, 70, 704
French, R., & Nicholson, P. 2000, Icarus, 145, 502
French, R. G., Salo, H., McGhee, C., & Dones, L. 2007a, Icarus, 189, 493
French, R. G., Verbiscer, A., Salo, H., McGhee, C., & Dones, L. 2007b, PAAS, 119, 623
Goldreich, P., & Tremaine, S. 1982, ARA&A, 20, 249
Hapke, B. W., et al. 2006, Lunar Planet Sci. Conf. XXXVIII, 1466
Hedman, M. M., Nicholson, P. D., Salo, H., Wallis, B. D., Buratti, B. J., Baines, K. H., Brown, R. H., & Clark, R. N. 2007, AJ, 133, 2624
Hernquist, L., Bouchet, F. R., & Suto, Y. 1991, ApJS, 75, 231
Hill, G. W. 1878, Am. J. Math., 1, 5
Irvine, W. M. 1966, J. Geophys. Res., 71, 2931
Julian, W., & Toomre, A. 1966, ApJ, 146, 810
Lumme, K., & Irvine, W. M. 1976, ApJ, 204, L55
Lyot, B. 1929, Annales de l'Observatoire de Paris, Section de Meudon, 8, 1, (English translation: NASA TT F-187 (1964))
Mishchenko, M., & Dlugach, Z. 1992, MNRAS, 254, 15P
Nelson, R. M., et al. 2006, Lunar Planet Sci. Conf. XXXVIII, 1461
Perrine, R. P., & Richardson, D. C. 2006, BAAS, 38, 560
Porco, C. C., Thomas, P. C., Weiss, J. W., & Richardson, D. C. 2007, Science, 318, 1602
Porco, C. C., Throop, H. B., & Richardson, D. C. 2001, BAAS, 33, 1091
Porco, C. C., Throop, H. B., & Richardson, D. C. 2003, BAAS, 35, 929
Porco, C. C., et al. 2004, Space Sci. Rev., 115, 363
Porco, C., et al. 2005, Science, 307, 1226
Reitsema, H. J., Beebe, R. F., & Smith, B. A. 1976, AJ, 81, 209
Richardson, D. 1994, MNRAS, 269, 493
Richardson, D., Quinn, T., Stadel, J., & Lake, G. 2000, Icarus, 143, 45
Richardson, D. C., Michael, P., Walsh, K. J., & Flyn, K. W. 2008, Planetary and Space Science, in press
Roques, F., Moncuquet, M., & Sicardy, B. 1987, AJ, 93, 1549
Salo, H. 1992, Nature, 359, 619
Salo, H. 1995, Icarus, 117, 287
Salo, H., & Karjalainen, R. 2003, Icarus, 164, 428
Salo, H., Karjalainen, R., & French, R. 2004a, Icarus, 170, 70
Shu, F. 1984, Planetary Rings, Waves in Planetary Rings (Arizona: Univ. of Arizona Press), 513
Squyres, S., & Veverka, J. 1981, Icarus, 46, 137
Stadel, J. 2001, PhD thesis, Univ. of Washington, Seattle
Supulver, K., Bridges, F., & Lin, D. 1995, Icarus, 113, 188
Tiscareno, M. S., Burns, J. A., Hedman, M. M., Porco, C. C., Weiss, J. W., Dones, L., Richardson, D. C., & Murray, C. D. 2006, Nature, 440, 648
Tiscareno, M. S., Burns, J. A., Nicholson, P. D., Hedman, M. M., & Porco, C. C. 2007, Icarus, 189, 14
Tomasko, M., & Doose, L. 1984, Icarus, 58, 1
van de Hulst, H. 1980, Multiple Light Scattering. Tables, Formulas and Applications (New York, NY: Academic)
Wadsley, J. W., Stadel, J., & Quinn, T. 2004, New Astron., 9, 137
Wisdom, J., & Tremaine, S. 1988, AJ, 95, 925
Zebker, H. A., Marouf, E. A., & Tyler, G. L. 1985, Icarus, 64, 531